1. Introduction

1.1. Background

The gravity field of Earth is a conservative field of force which is constantly changing. In essence, the gravitational potential at an external point is the sum of the gravitational potential, the potential of centrifugal forces and a varying component resulting from tidal effects from the Moon and Sun as well as from the motion of the Earth's poles. The strength and direction of the gravity field exhibits spatial-temporal variations. For example, due to the rotation of Earth, the Earth's gravity field at the poles is not the same as the gravity at the equator. Density, mass re-distribution and dynamics of the Earth's surface are often inferred from the gravity field and its spatial-temporal variability (Chen *et al*., 2005a). The gravity field of Earth plays a significant role in various fields of research such as geophysics, oceanography, hydrology, glaciology, geodesy and solid Earth science. In particular, the gravity field of Earth may be applied in geodynamics for example to observe time varying physical processes such as the post glacial uplift or sea level changes (Rummel *et al*., 2002). In geodesy, the gravity field of Earth may be used for precise satellite orbit determination (Rummel *et al*., 2002; Svehla and Rothacher, 2004).

The gravity field of Earth is often measured by use of geodetic satellite data collected from Satellite Laser Ranging (SLR) observations. These orbiting satellites are affected by both gravitational and non-gravitational accelerations (e.g. atmospheric drag, radiation pressure, etc.). During analysis of SLR observations, spatial-temporal variability and dynamics of the gravity field of Earth are inferred from analysing satellite orbit perturbations induced by the gravity field. A number of gravity field models (expressed as a set of coefficients consisting of a series expansion of spherical harmonics) have been derived since the mid 1960s by use of SLR tracking data and sometimes combined with terrestrial and altimeter data (e.g., Schwintzer *et al*., 1991, Lemoine *et al*., 1998, Foerste *et al*., 2006 and others). Accuracy of these models in terms of precise orbit determination (POD) depends on data availability, quality, type and geographical coverage.

The inherent biases in most of the existing gravity field models have not been extensively studied. These biases could be as a result of utilizing data from satellite missions that were not designed for gravity measurements. This is particularly true in cases where the

orbital parameters of the satellite in question are not suited for accurate gravity field recovery. In addition, SLR measurements often used for gravity field computation (i.e., time of flight measurements) are weather dependent. In most areas, approximately 50% of the time weather conditions such as cloud cover and rain do not allow for laser ranging. Furthermore, terrestrial gravity data and satellite altimeter data may also bias some of the gravity field models (e.g., the combined and tailored category of the gravity field models) since the geometry of the observations is not uniform (the data are not globally distributed). Difficulties in modelling the non-gravitational forces of most of the geodetic satellites (in particular the low Earth orbits) also limit the plausibility of achieving significant improvement in gravitational field modelling.

Nowadays the use of the on-board GPS/gradiometer receiver from the latest satellite missions (CHAMP, GRACE and GOCE) allows POD with unprecedented accuracy and almost complete spatial and temporal coverage. The data collected from these missions have resulted in the determination of a variety of new global gravity field models (e.g., EIGEN1, AIUB-CHAMP01S, EIGEN-CG04S, AIUB-GRACE01S, EIGEN-5C and many others) as well as updating the old gravity field models (e.g., EGM96 to EGM2008 and EIGEN-CG01C to EIGEN-CG03C, EIGEN-1S to EIGEN-6S, GGM02C to GGM03C, AIUB-GRACE01S to AIUB-GRACE013S). Today there are more than 100 global geopotential models (GGMs) derived by different research groups around the world. The ongoing development of geopotential models could be attributed to the availability of new data sets (with high quality and quick turn-around time) particularly from the recent advanced satellite missions as well as the SLR tracking data of multiple satellites.

Furthermore, development and improvement in gravity field modelling is anticipated as quantitative data become available in the future due to improvement of SLR technology. In particular, the employment of longer data spans from CHAMP, GRACE and GOCE with advanced processing software algorithms and empirical models are expected to increase the resolution and further improve the accuracy in gravity field models. Furthermore, the existence of numerous satellite missions not necessarily dedicated to gravity field research (e.g., COSMIC and SWARM missions) but equipped with space-borne GPS receivers are expected to contribute to the development of more accurate gravity field models (Prange *et al.*, 2008). These expectations however require that the accuracy and precision of existing gravity field models be assessed and validated. The research reported in this thesis focuses on investigating the accuracy

of different gravity field models using a new SLR analysis software package developed at Hartebeesthoek Radio Astronomy Observatory (HartRAO); it was named SLR Data Analysis Software (SDAS) by Combrinck (2010). The SDAS package was developed based on a modified spacecraft dynamics library provided by Montenbruck and Gill (2001). Some of its technical details are reported in Combrinck and Suberlyak, (2007). The software was designed by Combrinck (coding started in August 2004) and has been significantly updated and modified by him since the initial application report of 2007, and has been specifically modified to allow testing of different gravitational models.

1.2. Significance of the research

The International Laser Ranging Service (ILRS) has continued to make SLR observation data sets available to the scientific community (about four decades of data) since its formation in 1998. This service coordinates its operations, data dissemination and analysis through working groups, data and analysis centres. Unfortunately, none of the SLR analysis, lunar and associate analysis centres are in Africa. This research effort is a demonstration of preparedness towards the development of the first SLR analysis centre on the African continent. To analyse SLR data particularly for POD and geodetic parameter estimation only a few known software packages such as NASA/GSFC GEODYN II (Pavlis *et al*., 1999; Pavlis *et al*., 2006), NASA/GSFC SOLVE software, SATellite ANalysis (SATAN) software (Sinclair and Appleby, 1986), GFZ analysis software package EPOSOC and the University of Texas Orbit Processor (UTOPIA) are currently widely used by the analysis centres. However, the SDAS package (which is continuously updated and improved) will have to be augmented with several algorithms before it can be used to participate as an ILRS analysis centre, in order to produce standard analysis centre products, such as Earth Orientation Parameters (EOPs). These upgrades are in progress and new features are regularly added.

A number of gravity field models have been developed based on a combination of SLR, terrestrial and satellite altimeter data since the mid 1960s. The progressive development of gravity field modelling is often characterized by an improvement in spatial and temporal resolution and by the increased degree and order (of the spherical harmonics) of a geopotential field. Some of the new gravity field model developments (i.e. those models derived from CHAMP and GRACE satellite data) are followed by a validation phase that is often limited

spatially. Despite the continuous gravity field model development, research on the over-all accuracy of these models has not been reported. The present research contributes towards investigating the accuracy of some of the selected gravity field models and model categories (e.g. satellite-only, combined and tailored gravity field models). In general, the scientific contribution of the research reported in this thesis is particularly relevant to the SLR community, space geodesy and in general to Earth system science.

1.3. Aim and objectives

The overall aim of the present research is to study the accuracy of various gravity field models based on the SLR analysis software developed at HartRAO. In particular the LAser GEOdynamics Satellite (LAGEOS) 1 and 2 SLR data sets were considered in calculating the SLR range residuals i.e. the Observed-Computed (O-C) residuals. The specific objectives of this project were to:

- Analyse the historical development of gravity field models
- Calculate the range residuals using the SLR analysis software developed at HartRAO based on different geopotential models
- Investigate the accuracy of selected gravity field models using LAGEOS 1 and 2 data
- Investigate the contributions of Earth and pole tides on the O-C range residuals across selected gravity field models by use of different tide parameterization in the SDAS package.
- Compare the SDAS estimated J_2 with those published in the literature as well as investigating possible association of the J_2 coefficient with other geophysical parameters such as atmospheric and ocean angular momentum and the length of day.

1.4. Outline of the thesis

This thesis consists of seven chapters. In Chapter 2 an overview of space geodetic techniques is provided focussing on the SLR observational technique and its scientific applications. The data and methods used (analysis strategy) for data processing are described in Chapter 3. Chapter 4 contains the results of studies on the general improvement in gravity field modelling. In addition, results on the accuracy of gravity field models based on POD are presented. A

sensitivity analysis study is presented in Chapter 5. In Chapter 6 the J_2 coefficient estimated by the SDAS package from EGM96, GRIM5C1, GGM03C and AIUB-GRACE01S gravity field models is compared with the a priori J_2 for the four models. Furthermore, a linkage between J_2 and geophysical parameters, the length-of-day and atmospheric angular momentum was assessed. Lastly, Chapter 7 summarizes the research carried out, highlights research findings and provides recommendations for further research.

2. Space geodetic techniques and their data applications

To know the history of science is to recognize the mortality of any claim to universal truth, Evelyn Fox Keller, 1995.

2.1. Introduction

The launch of artificial satellites as early as 1957 has presented an unprecedented prospect of using the long period of available satellite data to study the size, shape and rotation of Earth as well as the variations in the Earth's gravity field. This is known as the three pillars of geodesy[1] (geokinematics, rotation and gravity field) in modern geodesy. In particular, the use of satellites for geodetic applications led to the development of satellite geodesy[2]. Satellite geodesy observations are achieved through space based techniques, particularly SLR and satellite positioning (e.g., Global Navigation Satellite Systems (GNSS)). The SLR technique measures the travel time (converted to range and corrected for a number of range delay parameters) of a transmitted laser pulse from the ground tracking station to the orbiting satellite in space and back to the ground station with an accuracy of approximately a centimetre. Applications of SLR measurements include the determination of the Earth's gravity field, monitoring of motion of the tracking station network with respect to the geocentre as well as calibration of geodetic microwave techniques (e.g. calibration of satellite orbits where the satellites are equipped with radar altimeters). On the other hand satellite based positioning and navigation systems, in particular the Global Positioning System (GPS), have opened unlimited possibilities for its use e.g. in geodetic control surveying and navigations (Seeber, 2003). For example, GPS data have been used for precise land navigation and have contributed to the establishment of precise geodetic control and the determination of GPS elevations above sea level.

Very Long Baseline Interferometry (VLBI), a technique which was developed in the late 1960's, has been broadly used in various fields of geodynamics such as global plate tectonic measurements and studies of variations in the Earth's rotation (Ryan *et al.*, 1993; Eubanks *et al.*, 1993). This technique has also resulted in the establishment and maintenance of an accurate and

[1] Geodesy can be defined as the science that determines the size and shape of the earth, the precise positions and elevations of points, and lengths and directions of lines on the Earth's surface, and the variations of terrestrial gravity (definition adopted from the International Association of Geodesy (IAG)).
[2] Satellite geodesy is a branch of geodesy which is concerned with satellite orbits, motion, perturbations and satellite based positioning (Seeber, 2003).

stable inertial (celestial) reference system which replaced the fundamental star catalogues. Here, a catalogue of Quasars (stable and distant radio sources) is used for defining the International Celestial Reference Frame (ICRF). The three techniques (SLR, GNSS and VLBI) together with Doppler Orbitography and Radio positioning by Satellites (DORIS) and even the Lunar Laser Ranging (LLR) technique, are the precise geodetic measurement methods and are often referred to as space geodetic methods or techniques (Koyama *et al.*, 1998). Space geodetic techniques are the fundamental tools for modern geodesy whose scope encompasses the provision of services to both society and the scientific community. Since these techniques have different characteristics in many aspects, it is preferred to collocate them (locate them on the same site) in order to compare the different and independently obtained results with each other thus improving their individual reliability. In this chapter the key space geodetic milestones are described and then a brief discussion of the principle and the main observables of the three space geodetic techniques (i.e., SLR, VLBI and GNSS) follow. A detailed focus is given to the SLR technique since it is used in this study. Here the discussion includes the properties of SLR, modelling factors that affect the accuracy of SLR measurements and some applications.

2.2. Milestones in space geodesy

Going back in history, geodesy together with its counterparts e.g. surveying, positioning and navigation merely meant measuring of angles as shown in Figure 1. To achieve such measurements the scale was roughly introduced by known distances between two sides of interest. Measurements using cross-staffs were often used to perform relative, local and absolute positioning (Beutler, 2004). A cross-staff is a mechanical device used to measure the angle between two objects (e.g., stars), see for example Figure 2. Historically the cross-staff was used in navigation to help sailors orient themselves, astronomers to study the sky, and by surveyors interested in taking accurate measurements. The cross-staff consists of a long pole with a series of markings and a sliding bar mounted at a perpendicular angle called a transom. To use a cross-staff, the navigator would position the end of the pole on the cheek just below the eye, and pick two objects to sight to, such as the horizon and the Sun. The navigator would then slide the transom along the cross-staff until one end lines up with one object and the opposite end lines up with the other object. Once the transom is in position, the marking covered by the transom

indicates the angle between the two objects, which can be used to calculate latitude and to collect other information.

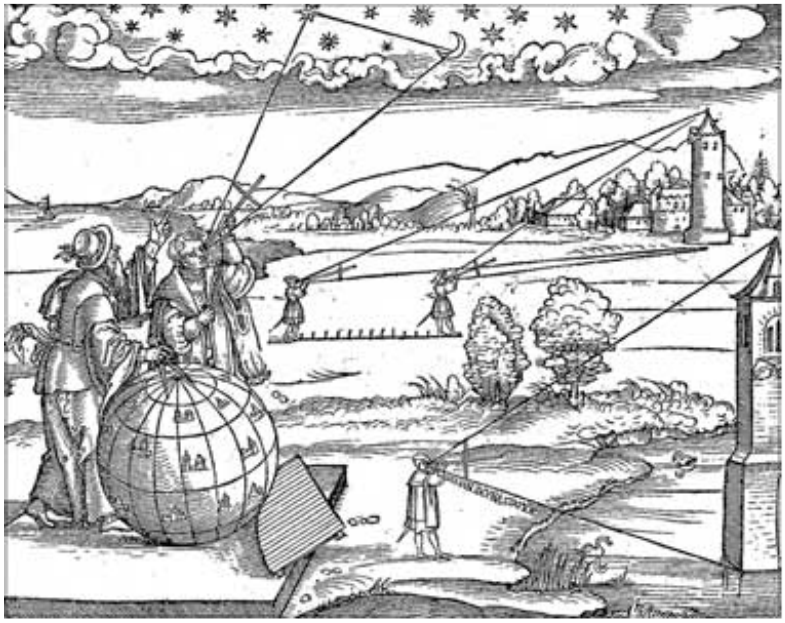

Figure 1. Historical technique of geodesy, surveying, positioning and navigation. Source: http://www.reformation.org.

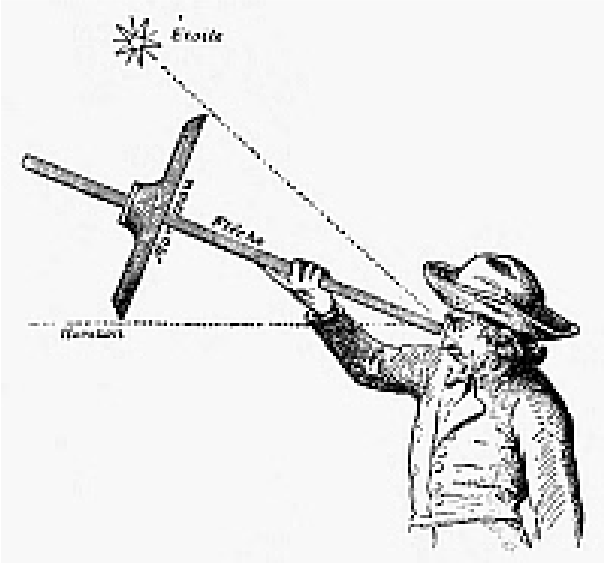

Figure 2. Cross-staff. Source: http://www.granger.com.

The geographical latitude of a site could be established by determining the elevation of the Sun or the polar star Polaris[3] and then looking up the latitude from a pre-calculated table. On the other hand, the longitude was determined by calculating the time difference between the unknown site and Greenwich (0° longitude). The time difference parameter was normally derived either by observing the Sun and measuring the local solar time or by observing certain stars and measuring their sidereal time. Problems related to the realisation of Greenwich time at the unknown observing time were solved by measuring lunar angular distances, lunar distances and angles between bright stars and the Moon. Increased accuracy in lunar orbit prediction allowed angular distances between the Moon and stars to be precisely predicted and tabulated in astronomical and nautical almanacs as a function of Greenwich local time (Beutler, 2004).

The development of new instruments such as marine chronometers (these are highly accurate clocks kept aboard ships and used to determine longitude through celestial navigation) resulted in dramatic improvement in navigation accuracy (Beutler, 2004). For instance, the cross-staff method was quickly replaced by more sophisticated optical devices which included telescopes. This innovative development allowed the determination of more accurate star fundamental catalogues and improvement in predicting motion of planets. Disciplines of fundamental astronomy emerged from the interaction between positioning, navigation, geodesy and surveying. Under such disciplines the terrestrial reference system was realized based on the geographical coordinates of a network of astronomical observatories with an accuracy of about 100 m (Beutler 2004). On the other hand the celestial reference frame was realized by using the derived-fundamental catalogues of stars. The transformation between the terrestrial reference and celestial reference frames enabled the monitoring of Earth rotation in inertial space and on the Earth's surface. Such monitoring revealed that the motion of the Earth's rotation exhibited short periodic variations. For example the Length-Of-Day (LOD) was noticed to slowly increase by about 2 ms per century. In addition, discoveries of the Earth's rotation axis moving on the Earth's surface (these are polar motion effects) were also reported in the literature. Historically, surveying and navigational equipment were too inaccurate to measure observables such as changes in LOD or polar motion, but as equipment and techniques improved, it was quickly

[3] Polaris is a bright star situated close to the North Celestial Pole (http://solar.physics.montana.edu). This type of star never rises or sets as the night progresses, but instead seems to be glued to the sky and is always in the North. So if one is lost in the Northern Hemisphere, one can always figure out direction by finding Polaris.

determined that the dynamics of the rotation of the Earth was not simply a case of undisturbed slow and predictable rotation.

The determination of the Earth's gravitational field also plays an essential role in geodesy and surveying. In the pre-space geodesy era, the gravity field of Earth was determined solely by *in situ* measurements on or near the surface of the Earth. Terrestrial instruments, which included gravimeters[4] and zenith cameras, were developed for gravity field measurements. These instruments however were suited for modelling the local as well as regional properties of the Earth's gravitational field. The desire to model the global properties of the gravity field of the Earth resulted in the development of satellite gravity missions. The use of artificial satellite missions led to the development of satellite geodesy (Kaula, 1966). Today there are four primary techniques, namely SLR, VLBI, GNSS and DORIS that are used in space geodetic observations for the purpose of studying the size, figure and deformation of the Earth and determination of its gravity field and the field's spatial and temporal variations. Apart from scientific interest, contributions from space geodetic techniques may also be applied in most societal areas ranging from disaster prevention and mitigation, to the provision of resources such as energy, water and food and also gaining an understanding of climate change.

2.3. Modern space geodetic techniques

Space geodetic techniques which include SLR, GNSS and VLBI and DORIS are fundamental tools of geodesy. Principles and properties of GNSS, VLBI and SLR methods are briefly reviewed in the following sections. For more information on DORIS the reader is referred to the following published literatures, Gambis (2004), Willis *et al*. (2006) and Coulot *et al*. (2007).

2.3.1. GNSS observable

Global Navigation Satellite System is a term used to describe a group of satellite based navigation systems that allow for the determination of positions anywhere on Earth. Currently the most commonly used GNSS consist of three main satellite technologies: the American controlled GPS, the Russian controlled Global Orbiting Navigation Satellite System (GLONASS) and the European GALILEO system. Each of these satellite systems consists

[4] A gravimeter is a specialized type of accelerometer designed for measuring the local gravitational field of the Earth (Zolfaghari and Gharebaghi, A., 2008).

mainly of three segments: (a) space segment, (b) control segment and (c) user segment (Aerospace Corporation, 2003). The GPS is the most utilized system for positioning, navigation and timing purposes and GPS satellites act as reference points from which receivers on the ground determine their positions. The navigation principle is based on the measurement of pseudo ranges between the user and at least three satellites. Ground stations precisely monitor the orbit of every satellite by measuring the travel time of the signals transmitted from the satellite distances between receiver and satellites. Resulting measurements include position, direction and speed.

In GNSS observations, measurements are often carried out using pseudo-range (or code range) and carrier phase. The primary observable is the phase measurement, which has applications in high precision positioning. Code or pseudo-range measurements are derived from the time difference between signal reception at receiver r and signal transmission at satellite, s. The time of signal transmission is equal to the time of reception less the signal travel time. Generally, the basic code observation equation is reported in Verhagen (2005) and is given by Equation (1)

$$P^{s}_{r,j}(t) = c\left[t_r(t) - t^{s}(t - \tau^{s}_{r,j})\right] + e^{s}_{r,j}(t), \qquad (1)$$

where $P^{s}_{r,j}$ is the code observation at receiver r from satellite s on frequency $j[m]$, t is the time observation in GPS time $[s]$, c is the speed of light in vacuum $[m/s]$, t_r is the reception time at receiver $r[s]$, t^{s} is transmission time from satellite $s[s]$, τ is the signal travel time $[s]$ and e the code measurement error. Since the receiver clock time and satellite clock time are not exactly equal to GPS time, the respective clock errors dt_r and dt^{s} ought to be accounted for as described in Equation (2)

$$t_r(t) = t + dt_{r(t)}$$
$$t^{s}(t - \tau^{s}_{r}) = t - \tau^{s}_{r,j} + dt^{s}(t - \tau^{s}_{r}). \qquad (2)$$

Substituting this Equation (1) yields

$$P^{s}_{r,j}(t) = c\tau^{s}_{r,j} + c[dt_r(t) - dt^{s}(t - \tau^{s}_{r})] + e^{s}_{r,j}(t). \qquad (3)$$

Correcting $\tau^{s}_{r,j}$ for instrumental delays at the satellite and the receiver as well as for atmospheric effects and multipath effects yield

$$\begin{aligned}\tau^{s}{}_{r,j} &= \delta\tau^{s}{}_{r,j} + d_{r,j} + d^{s}{}_{r,j} \\ \delta\tau^{s}{}_{r,j} &= \frac{1}{c}\left[\rho^{s}{}_{r} + da^{s}{}_{r,j} + dm^{s}{}_{r,j}\right],\end{aligned} \tag{4}$$

where $\delta\tau$ is the signal travel time from satellite antenna to receiver antenna $[s]$, d_r is the instrumental code delay in receiver $[s]$, d^s the instrumental code delay in satellite $[s]$, ρ the geometric distance between satellite and receiver $[m]$, $[da]$ the atmospheric code error and dm is the code multipath error $[m]$. With these corrections, the generalized code observation equation (see Verhagen, 2005) becomes

$$\begin{aligned}P^{s}{}_{r,j}(t) = \rho^{s}{}_{r}(t, t-\tau^{s}{}_{r}) + da^{s}{}_{r,j}(t) + dm^{s}{}_{r,j}(t) + \\ c[dt_r(t) - dt^{s}(t-\tau^{s}{}_{r}) + d_{r,j}(t) + d^{s}{}_{,j}(t-\tau^{s}{}_{r}] + e^{s}{}_{r,j}(t).\end{aligned} \tag{5}$$

Phase observation is a very precise but ambiguous measure of the geometric distance between a satellite and the receiver. Phase measurement equals the difference between the phase of the receiver-generated carrier signal at reception time, and the phase of the carrier signal generated in the satellite transmission time. The basic carrier phase observation equation is given by Equation (6)

$$\varphi^{s}{}_{r,j}(t) = \varphi_{r,j}(t) - \varphi^{s}{}_{r,j}(t-\tau^{s}{}_{r}) + N^{s}{}_{r,j} + \varepsilon^{s}{}_{r,j}(t). \tag{6}$$

Here φ is the carrier phase observation [cycles], N is an integer carrier phase ambiguity and ε is the phase measurement error. The phases on the right hand site simplify as expressed in Equation (7)

$$\begin{aligned}\varphi_{r,j}(t) &= f_j t_r(t) + \varphi_{r,j}(t_0) = f_j(t + dt_r(t)) + \varphi_{r,j}(t_0) \\ \varphi^{s}{}_{,j}(t) &= f_j t^{s}(t-\tau^{s}{}_{r}) + \varphi^{s}{}_{,j}(t_0) = f_j(t - \tau^{s}{}_{r,j} + dt^{s}(t-\tau^{s}{}_{r})) + \tau^{s}{}_{,j}(t_0).\end{aligned} \tag{7}$$

Here, f is the nominal carrier frequency $\left[s^{-1}\right]$, $\varphi_r(t_0)$ is the initial phase in the receiver at zero time [cycles] and $\varphi^s(t_0)$ is the initial phase in the satellite at zero time [cycles]. Inserting these expressions the carrier phase observation equation becomes

$$\varphi^{s}{}_{r,j}(t) = f_j\left[\tau^{s}{}_{r,j} + dt_r(t) - dt^{s}(t-\tau^{s}{}_{r}\right] + \left[\varphi_{r,j}(t_0) - \varphi^{s}{}_{,j}(t_0)\right] + N^{s}{}_{r,j} + \varepsilon^{s}{}_{r,j}(t). \tag{8}$$

Multiplying this equation with the nominal wavelength of the carrier signal

$$\phi_j = \lambda_j \varphi_j \qquad \text{with} \quad \lambda_j = \frac{c}{f_j}, \tag{9}$$

yields the carrier phase observation equation in meters as

$$\begin{aligned} \phi^s{}_{r,j}(t) = \rho^s{}_r(t, t-\tau^s{}_r) + \delta a^s{}_{r,j}(t) + c\left[dt_r(t) - dt^s(t-\tau^s{}_r) + \delta_{r,j}(t) + \delta^s{}_{,j}(t-\tau^s{}_r\right] \\ + \left[\phi_{r,j}(t_0) + \phi^s{}_{,j}(t_0)\right] + \lambda_j N^s{}_{r,j} + \varepsilon^s{}_{r,j}(t). \end{aligned} \tag{10}$$

2.3.2. The VLBI observable

Very Long Baseline Interferometry (VLBI) as a technique measures the delay in the arrival times of radio signals produced by a distant source being monitored simultaneously at two terrestrial antennas; see for example schematic representation in Figure 3. The time difference between the arrivals of the signal at each radio telescope is derived by correlation (at the correlator). These time delays and/or its derivative are used to calculate precisely the distance and direction of the baselines between the telescopes. Extragalactic objects that generate radio signals are often considered as point sources due to their great distance. In practice, for the purpose of geodetic VLBI, these sources (quasars) are carefully selected to ensure that they exhibit low proper motion and minimal source structure, so as to appear fixed and point-like. When this happens the time dependence of the time delay is generated via the Earth's motion, although it is dependent on the source location and the baseline vector between the two antennas.

In VLBI measurements the main observed quantities include the geometric delay, phase delay, group delay, the delay rate, and correlated amplitude. The geometric delay is directly related to the fringe phase as a function of frequency. It is as a result of the combination of the geometry of baseline and the direction to the radio source. Mathematically this delay observable can be described as in Tanir *et al.* (2006) and is expressed in Equation (11)

$$\tau_g = -\frac{1}{c}\vec{B}\cdot\vec{k}, \tag{11}$$

where c is the speed of light, $\vec{B}$ is the baseline vector between two stations and $\vec{k}$ is the unit vector towards the observed source. The baseline vector $\vec{B}$ can be transformed between the terrestrial geocentric system and celestial geocentric system. Such a transformation may be formulated as in Tanir *et al.* (2006) and is described as per Equation (12)

$$\vec{B}_c(t) = PNUXY\vec{B}_T(t). \tag{12}$$

In Equation (12) $\vec{B}_c(t)$ is the baseline vector in the celestial system and $\vec{B}_T$ is the baseline vector in the terrestrial system. In addition, (P,N,U,X,Y) represents a transformation term with respect to the Earth orientation parameters, e.g. precession and nutation model, a priori information for Earth rotation $(UT1)$ and polar motion (x_p, y_p). The baseline vector in the terrestrial reference frame takes into account corrections for: solid Earth tides, plate tectonics, ocean tide loading, atmospheric loading, hydrological loading, ionospheric correction, tropospheric correction and clock correction. Taking into consideration these corrections for geometric delay and transformation between the celestial and terrestrial system the geometric delay equation may be rewritten as

$$\tau_{obs} = -\frac{\vec{B}_T}{c} YXUNP\vec{k}_c + \tau_{tides} + \tau_{p.tect} + \tau_{o.load} + \tau_{h.load} + \tau_{ion} + \tau_{trop} + \tau_{clock} \ldots . \tag{13}$$

Here, τ_{obs} is the observed geometrical delay, B_T corresponds to the baseline vector in the terrestrial system and k_c is the source vector in the celestial system.

The phase delay is given by the ratio of the observed fringe phase and the reference angular frequency,

$$\tau_\phi = \frac{\phi_T}{2\pi\nu} + \frac{n}{\nu}. \tag{14}$$

where n is an unknown integer. The group delay is the derivative of the fringe phase with respect to angular frequency and is described by Equation (15)

$$\tau_G = \left(\frac{1}{2\pi}\right) \times \left(\frac{\partial \phi_T}{\partial \nu}\right). \tag{15}$$

The phase delay rate is defined as time rate of change of the phase delay and is given by Equation (16)

$$\dot{\tau} = \frac{\partial \tau_\phi}{\partial t} = \left(\frac{1}{2\pi\nu}\right) \times \left(\frac{\partial \phi_T}{\partial t}\right). \tag{16}$$

The correlated or visibility amplitude of the radio source signal is given by Equation (17)

$$V = \left(\frac{S_c}{S_t}\right). \tag{17}$$

Here, S_c is the correlated amplitude and S_t is the total amplitude or total flux.

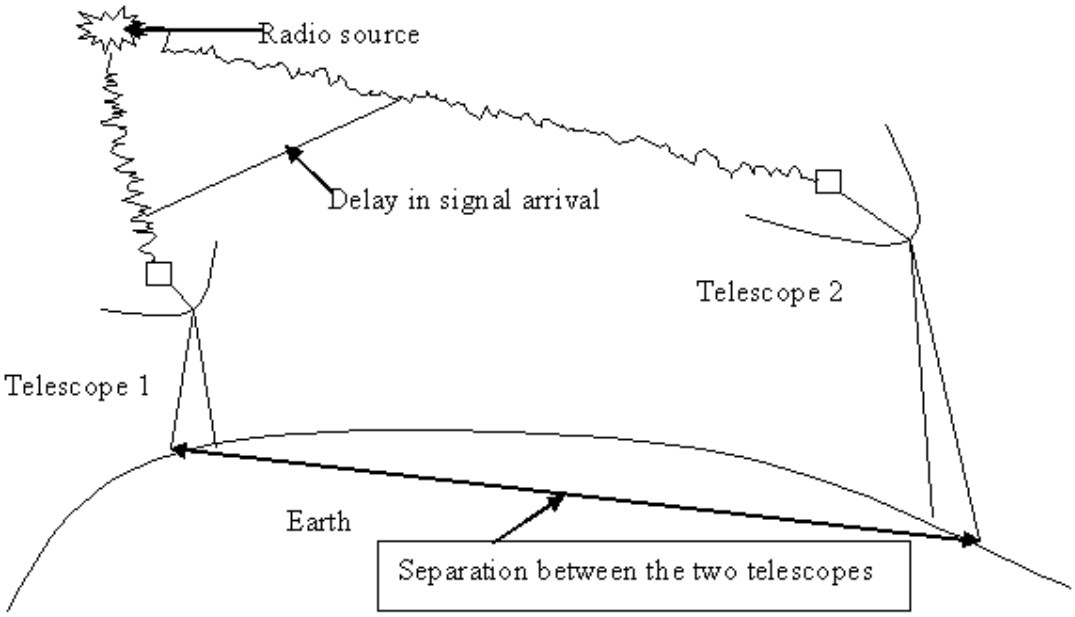

Figure 3. Schematic representation of VLBI concept.

2.3.3. SLR observable

Satellite Laser Ranging (SLR) is a technique that measures the two-way travel time of a short laser pulse which is reflected by an orbiting satellite. This method of measurement is applied to orbiting satellites equipped with special mirrors known as retro-reflectors (which are made from glass prisms). A schematic diagram illustrating the operation of a typical SLR system is presented in Figure 4. In a typical SLR system, a transmitting telescope emits short laser pulses with energy between 10 and 100 mJ at a pulse repetition frequency ranging between 5 and 20 Hz. Some modern systems have lower power levels and higher firing rates up to 2 kHz. The emitted laser pulse has a typical duration of two hundred or less picoseconds, most often specified by the Full Width Half Maximum (FWHM) of the pulse.

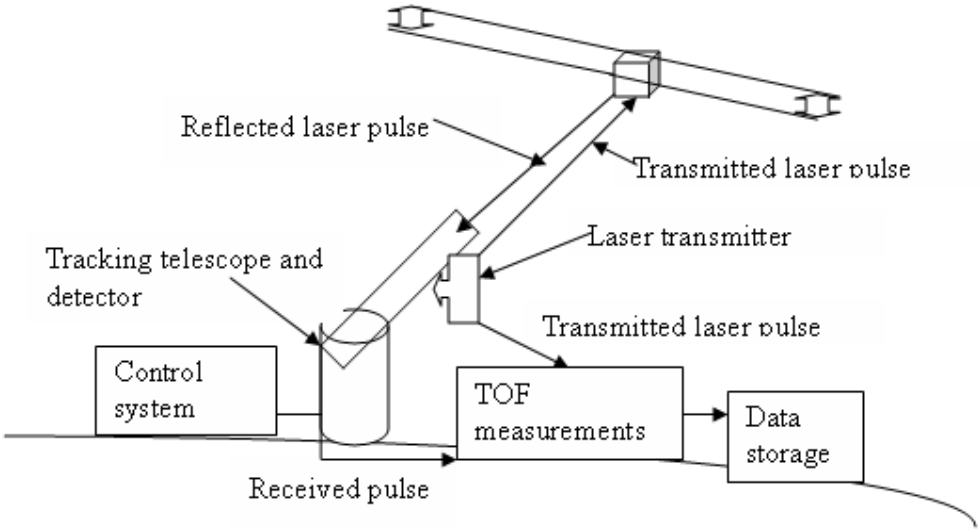

Figure 4. Schematic representation of a typical SLR system (adopted from Degnan, 1985).

Laser pulses propagate through the atmosphere to the orbiting satellite. Pulses which illuminate any of the retro-reflectors are reflected back through the atmosphere to the ground station were they are collected via the receiving telescope. The receiving telescope collects and focuses the reflected pulse energy onto a transmission photocathode (radiation sensor located inside a vacuum envelope of a photomultiplier) device of a photomultiplier (or a Single-Photon Avalanche Diode (SPAD)). A photomultiplier is a versatile and sensitive detector of radiant energy in the ultraviolet, visible, and near infrared regions of the electromagnetic spectrum.

When photons enter the glass vacuum tube, they impinge on the photocathode. The electron yield of this effect depends on the material of the cathode and is quantified as the ratio of emitted electrons to the number of incident photons. This is called the quantum efficiency, ε, and for SLR systems the efficiency is typically on the order of 10-15 percent (Degnan, 1985), a recently developed PMT with GaAsP photocathode and gating option (Hamamatsu R5916U-64) has a quantum efficiency of ~ 40% . Photoelectrons are emitted and directed by an appropriate electric field to an adjacent electrode or dynode within the envelope. As a result of the acceleration between the dynodes, the number of emitted electrons multiplies from step to step (this is similar to a cascading process). A number of secondary electrons are emitted at the dynode for each impinging primary photoelectron. These secondary electrons in turn are directed to a second dynode and so on until a final gain of perhaps 10^6 is achieved. The electrons

from the last dynode are collected by an anode which provides the signal current that is read out. This signal current which represents the round-trip Time-Of-Flight (TOF) of the pulse is stored by the system computer along with other information such as station positions and its velocities.

A basic equation representing an approximate TOF is given by Equation (18)

$$d = \frac{c \times t}{2}, \tag{18}$$

where c is the speed of light and t is the TOF. The speed of light is the signal propagation speed and a factor of two is included to reduce the round trip distance to the one way range. In order to obtain the best possible range precision[5] from the ground station to the satellite numerous corrections corresponding to internal delays in the transmission and detection systems are to be taken into account. Considering such parameter corrections Equation (18) can be expanded into Equation (19)

$$d = \frac{1}{2} c\Delta t + \Delta d_0 + \Delta d_s + \Delta d_b + \Delta d_r + \eta. \tag{19}$$

In Equation (19), Δt is the measured TOF and is mostly affected by uncertainties in the signal identification. The preferred resolution for the measured TOF is often a few picoseconds. In addition, the measured TOF needs to be tied to universal time (because of the satellite's motion relative to the Earth). The Δd_0 term corresponds to the eccentric correction on the ground, which is the intersection of the vertical axis and horizontal axis and is used as a reference point in the laser system. Similarly, Δd_s corresponds to the eccentric correction at the satellite and gives a geometrical relationship between the centre of each corner cube and the centre of mass (COM) of the satellite. The ILRS has COM corrections for different satellites and different laser frequencies (e.g. 1.01 m for AJISAI (Sasaki and Hashimoto, 1987) and 0.251 m for LAGEOS 2 (Minott *et al.*, 1993)). The Δd_b term in Equation (19) corresponds to the signal delay in the ground system. The geometric reference point and the electrical reference point is often not exactly at the same physical point; this correctional parameter is often determined through calibration with older systems that were calibrated with respect to a defined terrestrial target. The electrical delay and optical delay must be measured and constantly checked afterwards, to ensure that system dependent changes do not adversely affect measurement accuracies.

[5] Range precision refers to the degree of agreement of repeated measurements of the same property expressed quantitatively as the standard deviation computed from the results of a series of measurements.

Furthermore, Δd_r is the refraction correction as a result of atmospheric conditions which affect the propagation velocity of laser pulses. Laser pulses experience a delay in the lower part of the atmosphere, which makes measurements of these parameters along the total path difficult. Therefore atmospheric models are used that incorporate variables such as SLR site pressure and temperature and are supported by measured data at the laser site. Lastly, η are random systematic and observation errors related to un-modelled residual effects.

3.3.3.1. Historical development of SLR

The first SLR experiment campaign began in the 1960s with the development of the first (Ruby based) SLR station tracking satellites such Beacon Explorer-B (BE-B) (Osorio, 1992). Since then numerous satellite missions have been launched for different applications such as geodetic, Earth sensing and radio navigation and a global network of SLR stations has been established, replacing the old Baker-Nunn optical camera (Combrinck, 2010). A historical overview of such missions is summarised in Table 1.

Table 1. Timeline of artificial satellites which were tracked by global SLR stations.

Name	Launch date	Height (km)	Mission application
Starlette	1975	960	Gravity, tides, orbit determination
Lageos 1	1976	5900	Earth rotation, gravity, orbit, crustal deformation
Ajisai	1986	1500	Crustal deformation, gravity, orbit determination
Etalon 1/2	1989	19100	Crustal determination, Earth rotation
ERS-1	1991	780	Altimetry, orbit determination
Lageos 2	1992	5900	Crustal deformation, gravity, orbit determination
Stella	1993	810	Gravity, tides, orbit determination
ERS-2	1995	785	Altimetry, orbit determination
GFO-1	1998	800	Oceanography
CHAMP	2000	454	Gravity field, orbit determination
GRACE	2002	485	Gravity field, orbit determination
Larets	2003	691	Orbit determination
GOCE	2009	295	Gravity field, geoid

3.3.3.2. Global network of SLR stations

The current global network of SLR stations involved in artificial satellite tracking consists of over 40 stations and their global distribution is depicted in Figure 5. Most of the SLR tracking stations are located in the Northern Hemisphere leaving the Southern Hemisphere with weak

coverage. In Africa there are two stations, Helwan in Egypt and MOBLAS-6 (see Figure 6) located at HartRAO in South Africa. The space geodetic fundamental station HartRAO is involved with the International Laser Ranging Service (ILRS) activities as well as the other services of the International Association of Geodesy (IAG). This SLR tracking station is relatively isolated in Africa and more active than Helwan, hence plays a very important role as far as data coverage is concerned.

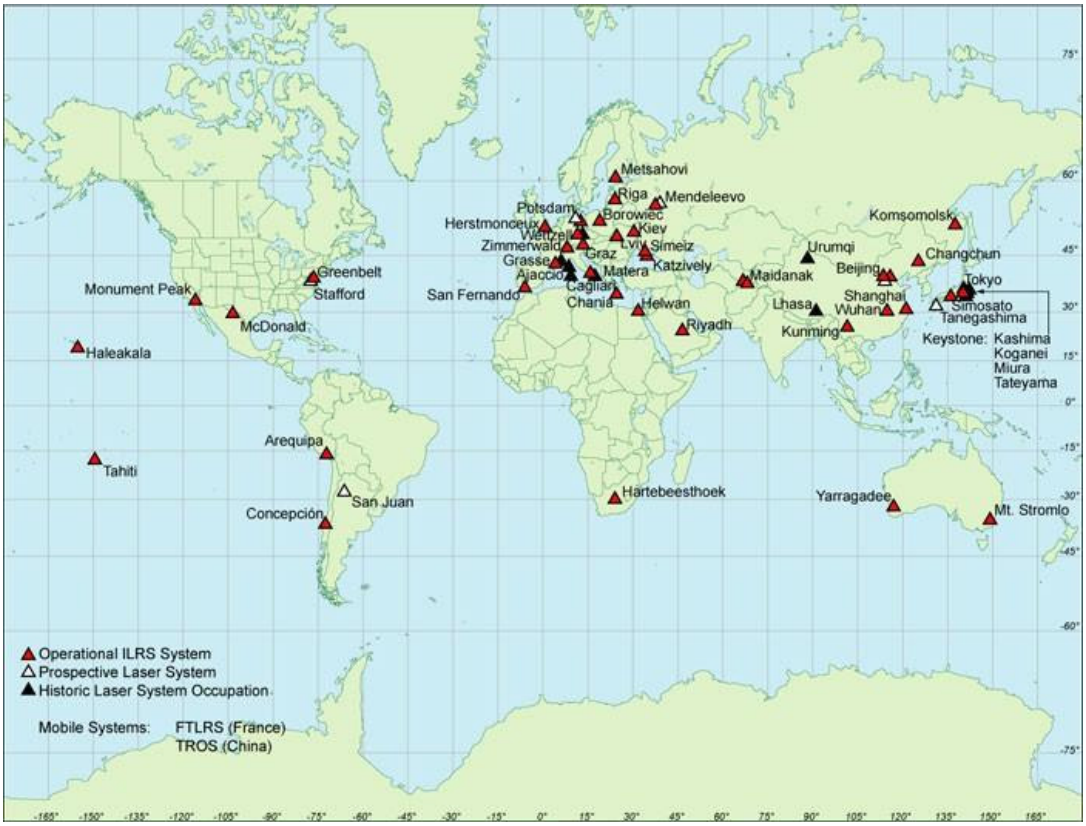

Figure 5. ILRS tracking network. Source: http://www.nasa.gov.

Figure 6. MOBLAS-6 at HartRAO. Source: http://www.hartrao.ac.za.

2.4. Modelling strategies in SLR

2.4.1. Forces acting on an orbiting satellite

2.4.1.1. Two-body problem

The two-body problem addresses the relative dynamics of two point masses attracted to each other by gravity. Its concept in SLR is primarily equivalent to modelling the forces of the motion between two gravitating masses, M and m (e.g., satellites around the Earth). In particular, the two-Body problem is founded on the assumptions that:

- the motion of the spacecraft is governed by attraction to a single central body,
- the central body and satellite are both homogeneous spheres or points of equivalent mass and
- only gravitational forces act on the bodies.

From Newton's law of gravitation, the force F on mass m orbiting about a spherically symmetrical body of mass M at distance r from the centre of mass is defined by Equation (20) as reported in Seeber (2003),

$$F = -\frac{GMm}{r^2}. \tag{20}$$

Here G is the gravitational constant.

Under the basic assumptions of the two-body problem the corresponding vector acceleration following Newton's second law of motion is given by Equation (21),

$$\ddot{r} = -\frac{G(M+m)}{r^3}\vec{r}, \tag{21}$$

where the vector from the centre of mass of the central body to the satellite is given by $\vec{r}$, M is the mass of the central body and m is the mass of the satellite. In addition, assuming that M is the main attracting mass and the mass of the satellite, m is extremely small such that compared to the central body M (e.g., $m \leq M$) the acceleration vector may be written as in Equation (22),

$$\ddot{r} = -\frac{GM}{r^3}\vec{r}. \tag{22}$$

Equation (22) can be solved through an analytical integration method to yield the position and velocity of mass m at future epochs. This is possible only if the initial conditions of position and velocity are known. In a case where perturbing forces act on an orbiting satellite then the satellite will experience additional accelerations due to the perturbing forces. In such case, the equation of motion may be written as in Equation (23),

$$\ddot{r} = -\frac{GM}{r^3}\vec{r} + \sum k_s, \tag{23}$$

where $\vec{r}$ is the position vector of the centre of mass of the satellite and k_s is a perturbing vector (which is in general the summation of all the perturbing forces acting on an orbiting satellite) and can be expressed as in Equation (24)

$$k_s = \bar{a}_g + \bar{a}_{ng} + \bar{a}_{emp}. \tag{24}$$

Here $\bar{a}_g$ is the sum of the gravitational forces acting on the satellite, $\bar{a}_{ng}$ is the sum of the non-gravitational forces acting on the surface of the satellite and $\bar{a}_{emp}$ represent the unmodelled forces which act on the satellite due to either a functionally incorrect or incomplete description

of the various forces acting on the satellite (Seeber, 2003). The gravitational forces, $\bar{a}_g$ acting on an orbiting satellite consist of a series of perturbations that are often expressed by Equation (25),

$$\bar{a}_g = \bar{P}_{geo} + \bar{P}_{set} + \bar{P}_{ot} + \bar{P}_{rd} + \bar{P}_{smp} + \bar{P}_{rel}, \tag{25}$$

where $\bar{P}_{geo}$ is the geo-potential force due to the gravitational attraction of the Earth, $\bar{P}_{set}$ and $\bar{P}_{ot}$ define perturbations due to solid Earth tides and ocean tides respectively, $\bar{P}_{rd}$ is due to rotational deformation of the Earth, $\bar{P}_{smp}$ are perturbations due to the Sun, Moon and planets and $\bar{P}_{rel}$ describes perturbations due to general relativity (Seeber, 2003). The non-gravitational forces acting on an orbiting satellite are given by Equation (26) as

$$\bar{a}_{ng} = \bar{P}_{drag} + \bar{P}_{solar} + \bar{P}_{earth} + \bar{P}_{thermal}. \tag{26}$$

Here $\bar{P}_{drag}$ is the atmospheric drag acting on a satellite, $\bar{P}_{solar}$ is due to solar radiation pressure, $\bar{P}_{earth}$ describes perturbation due to Earth radiation pressure (related to the albedo of Earth, typically 10% of the acceleration due to direct solar radiation pressure), $\bar{P}_{thermal}$ is the perturbation due to thermal radiation imbalance resulting from non-uniform temperature distribution on different satellite surfaces.

2.4.1.2. Gravitational field of the Earth

The Earth's gravity field is one of the most dominant forces that causes perturbations on an orbiting satellite. This force is often described in terms of spherical harmonic functions (Rapp, 1998). Harmonic functions may be defined as functions that satisfy Laplace's equation of the form given by Equation (27),

$$\nabla^2 U = 0. \tag{27}$$

In Equation (27), U represents a model of the Earth's gravity potential energy and ∇^2 is the Laplace operator expressed as in Equation (28),

$$\nabla^2 = \frac{\partial^2}{\partial x^2} + \frac{\partial^2}{\partial y^2} + \frac{\partial^2}{\partial z^2}. \tag{28}$$

Expressing the Laplace's equation in terms of spherical polar coordinates (where $x = r\sin\theta\cos\varphi$, $y = r\sin\theta\sin\varphi$ and $z = r\cos\theta$ with $r \in [0,\infty]$, $\theta \in [0,\pi]$ and $\varphi \in [0,2\pi]$) yields Equation (29) (Heiskanen & Moritz, 1967),

$$\nabla^2 U = \frac{1}{r^2}\frac{\partial}{\partial r}\left(r^2\frac{\partial U}{\partial r}\right) + \frac{1}{r^2\sin\theta}\frac{\partial}{\partial\theta}\left(\sin\theta\frac{\partial U}{\partial\theta}\right) + \frac{1}{r^2\sin^2\theta}\frac{\partial^2 U}{\partial\lambda^2} = 0. \qquad (29)$$

Here r is the Earth's geocentric radius, θ is the geocentric co-latitude and λ is the geocentric longitude. Equation (29) can be solved to obtain the gravity potential of the Earth in terms of spherical harmonics. For further details on how the gravity potential is derived from Equation (29), see Tapley *et al.* (2004a). In particular, the gravity potential can be expressed in the form described by Equation (30),

$$U(r,\varphi,\lambda) = \frac{GM}{r} + \frac{GM}{r}\sum_{n=2}^{N_{\max}}\sum_{m=0}^{l}\left(\frac{a}{r}\right)^l P_{nm}(\sin\varphi)\left[C_{nm}\cos m\lambda + S_{nm}\sin m\lambda\right]. \qquad (30)$$

Here, U is the gravity potential, GM is the Earth's gravity constant, (r,φ,λ) represent the magnitude of the radius vector, the latitude and the longitude respectively, n, m are the degree and order of spherical harmonics, P_{nm} are the Legendre functions and $\{C_{nm}, S_{nm}\}$ are the spherical harmonic (Stokes') coefficients (Tapley *et al.*, 2004a). The associated Legendre function for a given order m and degree n is defined by Equation (31),

$$P_{nm} = \left(1-x^2\right)^{m/2}\frac{d^m P_n(x)}{dx^m}, \qquad (31)$$

where $P_n(x)$ is the Legendre function which is expressed as a function of the independent variable x as depicted in Equation (32),

$$P_x(x) = \frac{1}{2^n n!}\frac{d^n}{dx^n}\left(x^2-1\right)^n. \qquad (32)$$

In most cases the spherical harmonic coefficients, $\{C_{nm}, S_{nm}\}$ are preferably given in normalized form, in which the order of magnitude remains approximately constant. This is due to the fact that these coefficients decrease numerically with large orders of magnitude with increase of degree and order of spherical harmonics. Computationally, these large differences could lead to round-off errors, although with modern computers and compilers, it is less a problem currently than say thirty years ago. In the SDAS software, any format is read (normalized or unnormalized) and converted to an internal (unnormalized) format for numerical processing.

The standard normalization factor is defined as in Equation (33) see Montenbruck and Gill (2001),

$$C_{nm} = \sqrt{\frac{(n-m)!(2n+1)(2-\delta_{0m})}{(n+m)!}}\,\bar{C}_{nm}, \tag{33}$$

and

$$S_{nm} = \sqrt{\frac{(n-m)!(2n+1)(2-\delta_{0m})}{(n+m)!}}\,\bar{S}_{nm}, \tag{34}$$

where C_{nm} and S_{nm} are the standard coefficients used in Equation (30), $\bar{C}_{nm}$ and $\bar{S}_{nm}$ are the normalized coefficients and $\delta_{0\mathrm{m}}$ is the Kronecker delta between 0 and m. For normalization purpose Equation (32) can multiplied by,

$$\begin{cases} \sqrt{(2n+1)}, & \text{if m=0 or} \\ \sqrt{2(2n+1)\dfrac{(n-m)!}{(n+m)!}}, & \text{if m} \geq 1. \end{cases} \tag{35}$$

Assuming that,

$$P_n^{(m)}(x) = \frac{d^m P_n(x)}{dx^m}. \tag{36}$$

In terms of the fully normalized coefficients, Equation (30) can be rewritten as in Equation (37),

$$U(r,\varphi,\lambda) = \frac{GM}{r} + \frac{GM}{r}\sum_{n=2}^{N_{\max}}\sum_{m=0}^{l}\left(\frac{a}{r}\right)^l \bar{P}_{nm}(\sin\varphi)\left[\bar{C}_{nm}\cos m\lambda + \bar{S}_{nm}\sin m\lambda\right]. \tag{37}$$

where, r is the geocentric radius of the computation point, $\{\bar{C}_{nm}, \bar{S}_{nm}\}$ are fully normalised spherical harmonic coefficients of degree n and order m, $\bar{P}_{nm}(\cos\theta)$ are fully normalized associated Legendre functions of degree n and order m. The spherical harmonics, $\{\bar{C}_{nm}, \bar{S}_{nm}\}$ may be classified as zonal (here, $m=0$ and the zeros of $\{\bar{C}_{nm}, \bar{S}_{nm}\}$ depict that the sphere is divided into latitudinal zones), sectorial (here $m=n$) and tesseral (in this case $m \neq n$). A typical example of zonal spherical harmonic functions is the J_2 coefficient which is equivalent to, $J_n = -J_{n0} = -\bar{C}_{n0}$. The J_2 (oblateness) coefficient is the main contributor of mass distribution near the Earth's polar axis causing the shape of Earth's rotation to deviate from a perfect sphere

(Montenbruck and Gill, 2001). Figure 7 illustrates some examples of spherical harmonic functions. A typical geopotential model is often described by these spherical harmonic coefficients.

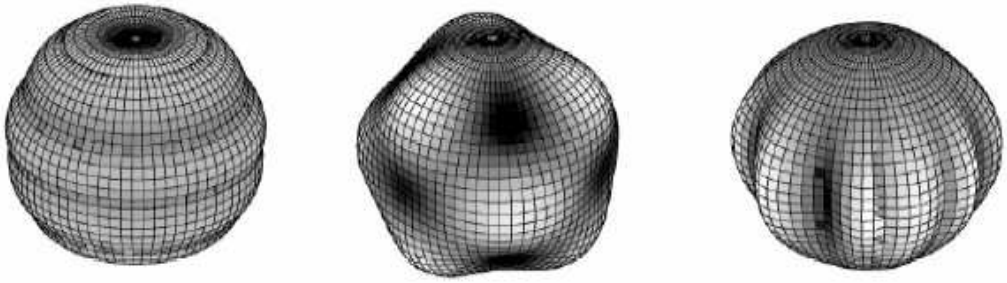

Figure 7. Examples of spherical harmonic functions of degree n and order m. (a) zonal (b) tesseral (c) sectoral (Laxon, 2003).

2.4.1.3. Third body effects

Satellites undergo acceleration originating from gravitational forces from the Sun, Moon and planets. These third body effects can dominate atmospheric drag effects in the case of high altitude satellites when the atmospheric drag effect begins to diminish. Generally, the effects from the three body perturbing forces are commonly described as per Equation (38) as reported in Tapley *et al*. (2004a),

$$\bar{P}_{smp} = \sum_{j=1}^{n_p} GM_j \left(\frac{\vec{\Delta}_j}{\Delta_j^3} - \frac{\vec{r}_j}{r_j^3} \right). \tag{38}$$

Here it is assumed that the gravity fields of the celestial bodies are perfect spheres. In Equation (38) j represents a specific body, GM_j denotes the gravitational parameter of each j, the position of the body j relative to the satellite is given by $\vec{\Delta}_j$, and $\vec{r}_j$ is the position vector of the body j relative to Earth.

2.4.1.4. Solid Earth tides

The solid Earth tides often manifest as an indirect effect from the attraction of Moon and Sun. They cause a deformation of the Earth's figure and therefore of the Earth's gravity field, which can be expressed as a deviation of the harmonic coefficients. The deviations of the Earth's

harmonic coefficients of the second and third order of spherical harmonics due to solid tides can be expressed by Equation (39) (McCarthy and Petit, 2003),

$$\Delta\bar{C}_{nm} - i\Delta\bar{S}_{nm} = \frac{k_{nm}}{2n+1}\sum_{j=2}^{3}\frac{GM_j}{GM_E}\left(\frac{R_e}{r_j}\right)^{n+1}\bar{P}_{nm}\left(\sin\Phi_j\right)e^{-im\lambda_j} \quad \left(\text{with } \bar{S}_{n0}=0\right). \qquad (39)$$

Here k_{nm} is the nominal degree Love number for degree n and order m, R_e is the equatorial radius of the Earth, GM_E is the gravitational parameter for the Earth, GM_j represents the gravitational parameters for the Moon $(j=2)$ and Sun $(j=3)$, r_j corresponds to the distance from geocentre to Moon or Sun, Φ_j is the body fixed geocentric latitude of Moon or Sun, λ_j corresponds to the Earth fixed east longitude (from Greenwich) of Moon or Sun and lastly, $\bar{P}_{nm}$ is the normalized associated Legendre function. The force acting on a satellite due to solid Earth tides is described by Equation (40),

$$\bar{P}_{set} = \sum_{j=1}^{2}\frac{k_2}{2}\frac{GM_{S,M}}{\vec{r}_{S,M}^{\,3}}\frac{a^5{}_E}{\vec{r}_{Sat}^{\,4}}\left[\left(3-15\cos^2\theta\right)\frac{\vec{r}_{sat}}{\vec{r}}+6\cos\theta\frac{\vec{r}_{S,M}}{r_{S,M}}\right]. \qquad (40)$$

In Equation (40), $\vec{r}$ is the radius vector of satellite (sat), Sun (S) and Moon (M), θ is the angle between radius vectors $\vec{r}_{sat}$ and $\vec{r}_{S,M}$, a_E is the equatorial radius of Earth, GM is the gravitational constant of the Sun and Moon.

2.4.1.5. Ocean Tides

The deformation of the Earth's gravity field caused by ocean loading tides can also be manifested in the deviations of the harmonic coefficients. A full description of equations describing the ocean tides model can be found in McCarthy and Petit (2003) and Petit and Luzum (2010). The equation describing ocean loading has been reported in McCarthy and Petit (2003) and Petit and Luzum (2010) and is given in Equation (41),

$$\Delta C_{nm} - i\Delta S_{nm} = F_{nm}\sum_{s(n,m)}\bar{\sum_{+}}\left(C^{\pm}{}_{snm} \mp S^{\pm}{}_{snm}\right)e^{\pm i\theta_f}, \qquad (41)$$

where,

$$F_{nm} = \frac{4\pi G\rho_w}{g}\sqrt{\frac{(n+m)!}{(n-m)!(2n+1)(2-\delta_{om})}}\left(\frac{1+k'_n}{2n+1}\right). \qquad (42)$$

Here g is mean equatorial gravity, k'_n is the load deformation coefficients, C_{snm}, S_{snm} are ocean tide coefficients for the tide constituent s, and θ is the argument of tide constituent s.

2.4.1.6. Pole tides

The pole tides given by Equation (43) are generated by the centrifugal effect of polar motion

$$\begin{aligned}\Delta v &= -\left(\frac{\Omega^2 r^2}{2}\right)\sin 2\theta\left(m_1\cos\lambda + m_2\sin\lambda\right)\\ &= -\left(\frac{\Omega^2 r^2}{2}\right)\sin 2\theta R_e\left[\left(m_1 - im_2\right)e^{i\lambda}\right],\end{aligned} \tag{43}$$

where $\left(m_1,\ m_2\right)$ are wobble variables. The deformation which constitutes the pole tide produces a perturbation given by,

$$-\frac{\Omega^2 r^2}{2}\,sin\,2\theta R_e\left[k_2\left(m_1 - im_2\right)e^{i\lambda}\right], \tag{44}$$

in the external potential. For the purpose of satellite orbit determination this perturbation is related to changes in the geopotential coefficients $\bar{C}_{21}$ and $\bar{S}_{21}$.

2.4.1.7. Relativistic effects

The relativistic correction to the acceleration of an orbiting satellite is commonly accounted as per Equation (45) recommended by the IERS 2003, published by McCarthy and Petit (2003) and Petit and Luzum (2010),

$$\begin{aligned}\Delta\ddot{\vec{r}} = \frac{GM_\oplus}{c^2 r^3}\Bigg\{&\left[2\left(\beta+\gamma\right)\frac{GM_\oplus}{r} - \gamma\left(\dot{\vec{r}}\cdot\dot{\vec{r}}\right)\right]\vec{r} + 2\left(1+\gamma\right)\left(\vec{r}\cdot\dot{\vec{r}}\right)\dot{\vec{r}}\Bigg\}.\\ &\left(1+\gamma\right)\frac{GM_\oplus}{c^2 r^3}\left[\frac{3}{r^2}\left(\vec{r}\times\dot{\vec{r}}\right)\left(\vec{r}\cdot\vec{J}\right) + \left(\dot{\vec{r}}\times\vec{J}\right)\right] + \left\{\left(1+2\gamma\right)\left[\dot{\vec{R}}\times\left(\frac{-GM_s\vec{R}}{c^2 R^3}\right)\right]\times\dot{\vec{r}}\right\}\end{aligned} \tag{45}$$

In Equation (45) the correction includes:

- first term, the non-linear Schwarzschild field of the Earth $\left(\approx 10^{-9}\ \mathrm{m\ s^{-2}}\right)$,
- second term, Lense-Thirring precession (frame dragging) $\left(\approx 10^{-11}\ \mathrm{m\ s^{-2}}\right)$,
- third term, de Sitter (geodetic) precession $\left(\approx 10^{-11}\ \mathrm{m\ s^{-2}}\right)$.

The approximate magnitude of acceleration presented here refers to LAGEOS as calculated by the SDAS package. In addition, c in Equation (45) is the speed of light, β, γ are the Parameterized Post Newtonian (PPN) parameters (these are parameters used to describe the classical tests of general relativity; in general relativity the two parameters are given by $(\beta,\gamma)=(1,1)$), $\vec{r}$ is the position of the satellite relative to the Earth, $\vec{R}$ is the position of the Earth relative to the Sun, $\vec{J}$ is the Earth's angular momentum per unit mass, $GM_{\oplus}$ is the gravitational coefficient of Earth and GM_s the gravitational coefficient of the Sun. Although the effects of these parameters are very small for the purpose of POD they need to taken into account as there are some long-term periodic and secular effects in the orbit (Huang and Liu 1992).

2.4.1.8. Solar radiation pressure

Solar radiation pressure describes an exchange of momentum between photons absorbed and reflected by the surfaces of an orbiting satellite (Ziebart, 2001). This conveyed force causes acceleration which is dependent on the solar flux, the satellite's mass m and cross-section A. According to Montenbruck and Gill (2001), the solar radiation pressure contributions to the total perturbative acceleration is described as per Equation (46),

$$\bar{P}_{solar} = -\nu P_e C_R \frac{A}{m}\frac{\vec{r}_e}{r_e^3} AU^2. \qquad (46)$$

where P_e is the radiation flux from the Sun, $\vec{r}_e$ is the geocentric position of the Sun, C_R is the reflection coefficient $(C_R = 1.13)$ and ν is the eclipse factor and it determines the amount of solar radiation acting on the satellite as it passes through umbra and penumbra regions. The conditions for the eclipse factor functions are $\nu = 0$ if the satellite is in the shadow region (umbra phase), $\nu = 1$ if the satellite is in full sunlight and $0 < \nu < 1$ if the satellite is in partial shadow (penumbra phase).

2.4.1.9. Atmospheric drag

Satellites orbiting the Earth at low Earth altitude are also affected by drag force (the component of the resultant dynamic fluid force that acts in opposition to the relative motion of the object with respect to the fluid) (Montenbruck and Gill, 2001). Although the air density is extremely low at altitudes higher than 1000 km, the high velocity of a satellite often leads to significant (de-)acceleration. The acceleration due to air drag can be obtained by Equation (47) according to Montenbruck and Gill (2001),

$$\bar{P}_{drag} = -\frac{1}{2} C_D \frac{A}{m} \rho v_r^2 \vec{e}_v . \tag{47}$$

Here, C_D is a dimensionless quantity describing the satellite's interaction with the atmosphere (also referred to as the satellite's drag coefficient); m is the total mass of the satellite; $\vec{e}_v = \vec{v}_r / v_r$ is a unit vector describing the direction of the acceleration due to drag and is anti-parallel to the satellite velocity vector; v_r is the magnitude of the satellite's velocity relative to the atmosphere; A is the projected area in the direction of the velocity vector relative to the atmosphere and lastly, ρ the atmosphere's mass density.

2.4.2. Tropospheric delay modelling

SLR observations are highly affected by the residual errors arising from inaccurate modelling the effect of delay of the signal propagation through the neutral atmosphere (i.e., the troposphere and stratosphere). Early atmospheric correction models used during SLR analysis include one developed by Marini and Murray (1973). Later, the shortcomings of Marini and Murray's atmospheric model (e.g., inaccurate mapping function component of the model) were pointed out by Mendes *et al.* (2002). Today, mapping functions derived by Mendes *et al.* (2002) are widely used in combination with any zenith delay (ZD) model to predict atmospheric delay in the line-of-sight direction.

In general, the atmospheric delay contribution is described by McCarthy and Petit (2003) and is expressed here by Equation (48),

$$d_{atm}^{z} = 10^{-6} \int_{r_s}^{r_a} N dz = \int_{r_s}^{r_a} (n-1)\, dz. \tag{48}$$

Splitting the ZD into hydrostatic $\left(d_h^z\right)$ and non-hydrostatic $\left(d_{nh}^z\right)$ components, Equation (48) can be rewritten as described by Equation (49),

$$d_{atm}^z = d_h^z + d_{nh}^z = 10^{-6}\int_{r_s}^{r_a} N_h dz + 10^{-6}\int_{r_s}^{r_a} N_{nh} dz. \tag{49}$$

In Equation (49), $N = (n-1)\times 10^6$ is the total group refractivity of moist air, n is the total refractivity index of moist air, N_h and N_{nh} are the hydrostatic and non-hydrostatic components of the refractivity, r_s is the geocentric radius of the laser station, r_a is the geocentric radius of the top of neutral atmosphere, and d_{atm}^z and dz have length units.

According to Mendes and Pavlis (2004) the hydrostatic ZD can be expressed as in Equation (50),

$$d_h^z = 0.002416579\frac{f_h(\lambda)}{f_s(\phi,H)}P_s, \tag{50}$$

where d_h^z is the zenith hydrostatic delay in meters, and P_s is the surface barometric pressure in hPa. The function $f_s(\phi,H)$ in Equation (50) can be expressed as in Equation (51).

$$f_s(\phi,H) = 1 - 0.00266\cos 2\phi - 0.00000028H. \tag{51}$$

Here ϕ is the geodetic latitude of the station and H is the geodetic height of the station in meters. The dispersion equation for the hydrostatic component is described by Equation (52)

$$f_h(\lambda) = 10^{-2}\times\left[k_1^*\frac{\left(k_0+\sigma^2\right)}{\left(k_0-\sigma^2\right)^2} + k_3^*\frac{\left(k_2+\sigma^2\right)}{\left(k_2-\sigma^2\right)^2}\right]C_{CO_2}. \tag{52}$$

In Equation (52), $k_0 = 238.0185\ \mu\text{m}^{-2}$, $k_2 = 57.362\ \mu\text{m}^{-2}$, $k_1^* = 19990.975\ \mu\text{m}^{-2}$, and $k_3^* = 579.55174\ \mu\text{m}^{-2}$, σ is the wave number, with $\sigma = \lambda^{-1}$, where λ is the wavelength in μm, $C_{CO_2} = 1 + 0.534\times 10^{-6}(x_c - 450)$, where x_c is the carbon dioxide (CO_2) content in parts-per-million (ppm). The expression for non-hydrostatic ZD expressed as in Equation (53),

$$d_{nh}^z = 10^{-4}\left(5.316 f_{nh}(\lambda) - 3.759 f_h(\lambda)\right)\frac{e_s}{f_s(\phi,H)}, \tag{53}$$

where d_{nh}^{z} is the zenith non-hydrostatic delay in meters, and e_s is the surface water vapour pressure in nPa. The dispersion expression for the non-hydrostatic component is given by Equation (54),

$$f_{nh}(\lambda) = 0.003101\left(w_0 + 3w_1\sigma^2 + 5w_2\sigma^4 + 7w_3\sigma 6\right), \tag{54}$$

where $w_0 = 295.235$, $w_1 = 2.6422\ \mu m^2$, $w_2 = -0.032380\ \mu m^4$, and $w_3 = 0.004028\ \mu m^6$. Marini and Murray (1973) have demonstrated that if the atmosphere is assumed to be azimuthally symmetric then the mapping functions for the atmospheric delay are asymptotic in $\sin(\varepsilon)$ near zenith and inverse in $\sin(\varepsilon)$ near the horizontal. The azimuthally symmetric mapping function and the hydrostatic gradient can be calculated from the geopotential heights. In the case where the wet mapping function is not in hydrostatic equilibrium, the vertical distribution of refractivity due to water vapour is utilized. Here the adopted parameters need to reflect both the vertical distribution as well as the changing geometry with height above the surface due to the curvature of the Earth. The adopted parameter for both the hydrostatic and wet mapping functions is a single input along with the site geographic location. The mapping function of a truncated continued fraction in $1/\sin(\varepsilon)$ can be described as per Equation (55) as reported in McCarthy and Petit (2003),

$$m(\varepsilon) = \frac{1 + \dfrac{a}{1 + \dfrac{b}{1+c}}}{\sin\varepsilon + \dfrac{a}{\sin\varepsilon + \dfrac{b}{\sin\varepsilon + c}}}. \tag{55}$$

In Equation (55), $m(\varepsilon)$ is the mapping function, ε is the vacuum elevation of the incoming ray and a, b and c are the coefficients of the mapping function which depend on integrals refractivity through the atmosphere.

2.5. Applications of SLR measurements

2.5.1. International Terrestrial Reference Frame (ITRF)

The SLR observations, in particular from LAGEOS 1 and 2 have played a significant role in providing data that have been used for the establishment of the ITRF[6] (McCarthy and Petit, 2003). The ITRFs are realized through computing global Cartesian coordinates and geophysical parameters such as station coordinates (positions and linear velocities) and Earth Orientation parameters (EOP) (McCarthy and Petit, 2003 and Petit and Luzum, 2010). These coordinates form a single solution which is sent to the International Earth Rotation and Reference System (IERS) where it is used to determine a unique solution of the ITRF. Single solutions from other space geodetic techniques such as GPS, VLBI and DORIS may be combined with the solution from SLR observations to form a four-in-one solution which can then be used to determine, maintain and improve the ITRF precisely**.** In addition, the four-in-one solution provides a unique solution for the measurements of the EOP which are used to describe the irregularities of the Earth rotation with respect to a non-rotating reference frame as well as for satellite positioning (Gambis, 2004).

Generally, the EOP are formed by five components: the X and Y polar motion with respect to the crust, Universal Time (UT1), a nutation correction in ecliptic longitude $(d\varphi)$, and a nutation correction in obliquity $(d\varepsilon)$. Today, the two nutation corrections can be precisely modelled to an accuracy of about 3 cm for about a one year period (Oliveau and Freedman, 1997). The UT1 parameter may be defined as a measure of the angular rotation of the Earth about its spin axis and is usually specified with respect to a reference time defined by atomic clocks (e.g., UT1–UTC) (Freedman *et al*., 1994). This parameter together with X and Y polar motion are known to exhibit rapid variations and are also unpredictable in time. The random variations are due to the interaction of the atmosphere and the crust (Freedman *et al.* 1994) while the UT1 often varies more rapidly than polar motion.

The difference between the astronomically determined duration of the day and 86 400s of International Atomic Time (TAI) is known as the Length-Of_Day (LOD) and is often derived

[6] The ITRF is a set of physical points with precisely determined coordinates in a specific coordinate system attached to the International Terrestrial Reference System (ITRS) (McCarthy and Petit, 2003).

from the UT1 series as a temporal rate of change of the difference (UT1-TAI). The excess LOD, denoted by A is related to the UT1 rate of change given by Equation (56),

$$A = -A_0 \frac{du}{dt}, \tag{56}$$

where A is the excess LOD and A_0 is the nominal LOD (86 400 seconds). When modelling the stochastic behaviour of UT1 and LOD the effects of physical processes (e.g., solid Earth and ocean tides) which influence the rotation rate ought to be taken into account. Such effects can be removed from the two EOP components by applying corrections obtained from conventional tidal models (Yoder *et al.*, 1981). The Earth orientation changes often represented by polar motion, X, Y, the equatorial components in a geographical reference frame, and variations in the LOD (see Figure 8 for variations in LOD and excitations in X and Y polar motion) are often explained by studying variations of atmospheric and/or oceanic angular momentum. Such variations are caused by the exchange of angular momentum between the solid Earth and its geophysical fluid envelope. Eubanks *et al.* (1993) found that variations in the Earth's rate of rotation which corresponds to changes in LOD amount to a few parts in 10^8. Studies by Ponsar *et al.* (2003) suggested that the variations in LOD are caused by interaction between the Earth's core and mantle. Similar studies by Gross *et al.* (2003) related the LOD variations with tidal variations exhibiting periods between 12 hours and 18.6 years. Such variations were believed to be due to the deformation of solid Earth and changes in the strength and direction of the atmospheric winds.

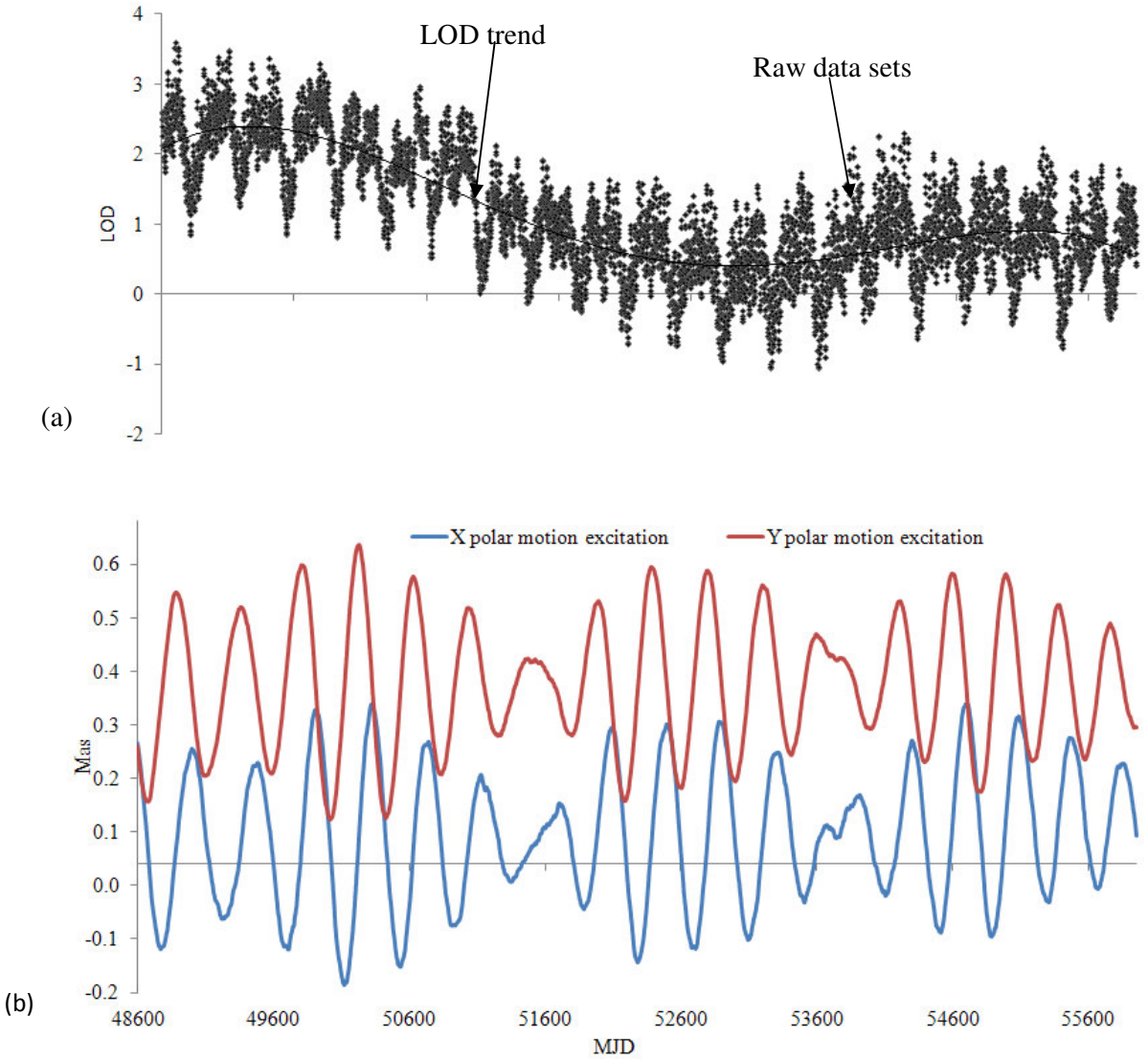

Figure 8. Time series (in Modified Julian Date (MJD)) of Earth rotation extracted from SLR data. (a) LOD variations, (b) X and Y polar motion excitation, data obtained from http://www.iers.org/IERS archive.

2.5.2. Gravity field

Satellite Laser Ranging tracking data have been used to determine the Earth's gravity field both at global and regional scales. Since the orbital motion of artificial satellites is influenced by gravitational forces, precise satellite tracking measurements provide orbit solutions which can be inverted to derive the gravity field. For instance, the long wavelength gravity information can be derived through SLR range measurements by high altitude satellites such as LAGEOS.

However, gravity field determination to higher degree of coefficients using SLR experiences certain drawbacks due to unsteady and fragmentary orbit tracking by ground stations. The recent satellite missions, e.g. CHAMP, GRACE and GOCE are designed to overcome the existing SLR disadvantages. Nowadays the gravity field determination is achieved based on three techniques in the context of CHAMP, GRACE and GOCE satellite missions (Tapley *et al*. 2004b). These techniques include a continued GNSS tracking using on-board GPS receivers and accelerometers for measuring non-gravitational forces such as atmospheric drag and solar radiation pressure. The GRACE satellite is additionally equipped with a K-band microwave system (known as K-band range-rate technique), which measures their separation range-rate with significant accuracy (Tapley *et al*. 2007). This technique is believed to be the most important in terms of gravity field determination for the on-board GRACE mission. Satellite gradiometry equipped on the GOCE mission is the most recent technique used for gravity field determination and non-gravitational accelerations acting on the satellite (Pail *et al*. 2011). The on-board GOCE gradiometer determines the position and velocity of the satellite and is used for estimation of the long wavelength signal of the gravity field. Low-altitude satellites, however, are subjected to non-gravitational forces, particularly from the atmosphere, and these can affect the gravity inversions at all wavelengths.

According to Newton's law, changes in the gravity field are a manifestation of mass redistribution in the Earth system. Any movement of masses in, on or above the Earth will therefore introduce variations in the gravity field of the Earth (Dickey *et al*., 2002; Cox *et al*., 2003). Temporal variations of Earth's gravity field may range between 10 and 100 ppm (variation from the mean) and often occur on a variety of time scales (ranging from hours to thousands of years) (Tapley *et al*., 2004b). Such variations are caused by a variety of phenomena that redistribute mass, including tides raised by the Sun and Moon, and post-glacial rebound. Surface mass change in the atmosphere, oceans, hydrosphere and cryosphere are dominated by seasonal and inter-annual variations while processes such as isostatic glacial recovery and sea-level change give rise to long-term secular or quasi-secular signatures.

Several studies have investigated the long term and the seasonal variations of the Earth's gravity field using data collected from different satellite missions. In particular, the lower order harmonic component of the gravity field with $n=2$ and $m=0$ (hereafter J_2) which characterizes the oblateness of the Earth has attracted a lot of interest from the scientific

community. Early studies of J_2 by for example Yoder *et al*. (1983) showed a secular decrease in J_2 that was consistent with a steady migration of mass from low latitudes towards high latitudes resulting in a linearly decreasing trend. Such a trend was thought to be related to post-glacial rebound (PGR), the Earth's ongoing response to the removal of the ice loads at the end of the last ice age. Long term studies by Cox and Chao (2002) however discovered that J_2 started to increase around 1997, but later exhibited a negative trend (from 2002) as illustrated in Figure 9. This trend is believed to have inverted again with J_2 once more decreasing. Several mechanisms have been suggested to be the causes for this sudden change of the J_2 coefficient. For example, Dickey *et al*. (2002) attributed this change to the surge in sub-polar glacial melting and to mass shifts in the Southern, Pacific, and Indian oceans. In addition to the increasing trend of the J_2 coefficient, Nerem *et al*. (2000) found that the J_2 coefficient might be exhibiting seasonal variability due to a combination of atmospheric pressure variations and variations in the distribution of water in the oceans and on land. Furthermore, Dickey *et al*. (2002) detected inter-annual variability in J_2 which they attributed to climatically driven oscillations in the ocean, storage of water, snow, and ice on land and partly as a result of the effects of anelasticity on the 18.6-year solid Earth tide as suggested by Benjamin, *et al*. (2006).

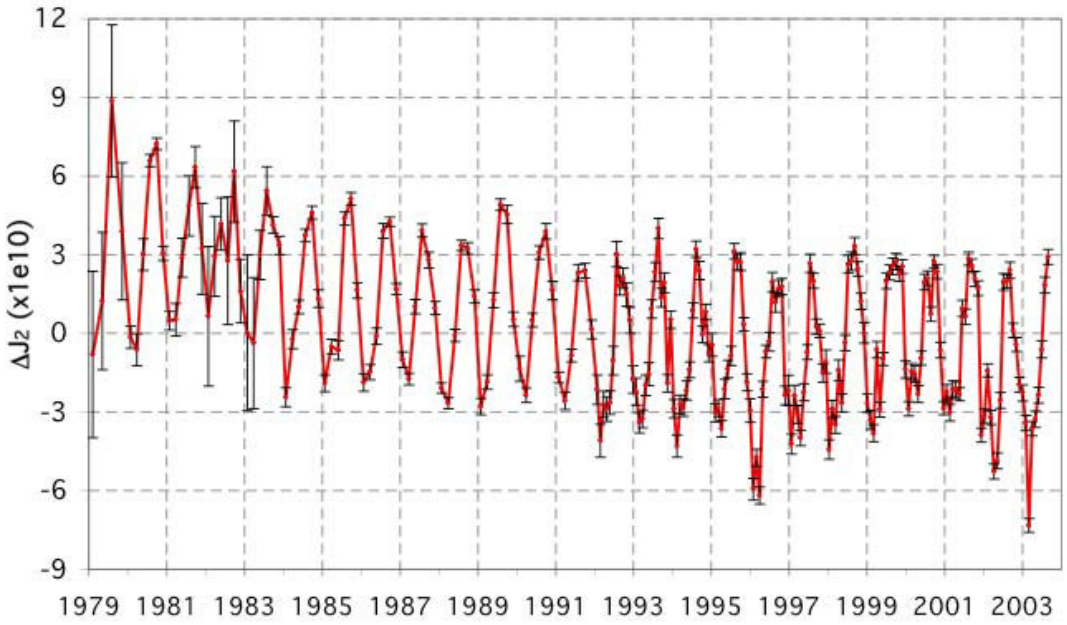

Figure 9. The variability of J_2 coefficient as derived from SLR and DORIS data spanning the period from 1976 to 2006 (Cox and Chao, 2002).

2.5.3. Determination of the geoid

Data from SLR observations have been used for computation of spherical harmonic models. These models can be used to derive the geoid (this is the equipotential surface of the Earth's gravity field that corresponds closely with Mean Sea Level (MSL) in the open oceans, ignoring oceanographic effects) as well as the geoidal height (the separation between the geoid and the ellipsoid) (Eckman, 1998). The geoidal height is often computed from a set of normalized spherical coefficients using Equation (57),

$$N_{GM} = \frac{GM}{r\gamma}\sum_{n=2}^{N_{max}}\left(\frac{a}{r}\right)^n\sum_{m=0}^{n}\left\{\bar{C}^*_{nm}\cos m\lambda + \bar{S}_{nm}\sin m\lambda\right\}\bar{P}_{nm}(\cos\theta). \qquad (57)$$

Here n_{max} is the maximum degree at which the coefficients are known, $\bar{C}^*_{nm}$ are the $\bar{C}_{nm}$ less the zonal coefficients of the normal potential of the selected reference ellipsoid, γ is the normal gravity on the surface of the reference ellipsoid and the rest of the parameters are as given in Equation (37). Determination of the geoid has been one of the main research areas in Geodesy for decades. To this end, geoid heights at any points on the Earth's surface can be determined with accuracy ranging from 30 cm to a few meters (Rapp, 1998). A number of researchers have

addressed the precise determination of geoid height on a local and regional scale for oceanographic and geophysical applications. At a local scale, the geoid can be determined by a combination of GPS derived heights and levelled heights, through gravimetric and geometric approaches. From the GPS derived heights and levelled heights at some points, the geoid heights at these points can be calculated. At a local scale the geoid height measurements are often converted to gravity anomalies or deflections of the vertical (e.g., geoid slope). Several global geoid height and gravity anomaly models have been developed from tracking and modelling the orbits of numerous artificial satellites (Dawod, 2008; Featherstone and Olliver, 2001; Kiamehr and Sjoeberg, 2005).

Global gravity change has also attracted particular attention in the scientific community as it is often related to global sea-level changes. The sources of global sea-level rise often involve the redistribution of mass from the continents to the ocean. The usage of gravity field measurements allows for discrimination between several sources through the continuous monitoring of geoid changes on both global and regional scales as well as on basin scales. Gravity field solutions can be used to numerically estimate components such as thermal expansion (eustatic) and fresh water influx which influence global sea level changes (Cazenave and Nerem, 2004; Jevrejeva *et al*., 2006). Measurements of temporal gravity variations can be also used to determine water storage change in the hydrological system. In particular, since the launch of the GRACE mission in 2002, numerical articles assessing the potential of GRACE recovering hydrological signals have been published. For example, Andersen and Hinderer (2005a) have investigated the potential of inferring inter-annual gravity field changes caused by continental water storage change, as determined from GRACE observations between 2002 and 2003. Contributions from continental water storage change were compared to the output from global hydrological models. Andersen *et al*. (2005b) and Neumeyer *et al*. (2006) correlated large scale hydrological events with the estimated change in the gravity field for certain areas of the world to an accuracy of 0.4 μGal, corresponding to 9 mm of water. On a regional scale, Winsemius *et al*. (2006) compared hydrological model outputs for the Zambezi river basin with estimates derived from GRACE. Monthly storage depths produced by the hydrological model displayed larger amplitudes and were partly out of phase compared to the estimates based on GRACE data.

2.5.4. Precise satellite orbit determination

Precise satellite orbit determination is one of the most essential applications of SLR observations. It involves the estimation of position and velocity of an orbiting satellite at a specific time epoch (Yunck, 1997). Satellite orbit determination is used for geo-location of the satellite sensors and to measure the gravity field and its variations in time. There are currently three ways in which satellite orbit can be calculated, namely: dynamic, kinematic and reduced-dynamic.

2.5.4.1. Dynamic orbit determination

The dynamic orbit determination (Yunck, 1997) utilizes a set of tracking observations and mathematical models that describe the forces acting on an orbiting satellite. Here the force and satellite models are used to compute a model of satellite acceleration over a given time. The acceleration model describes the satellite's instantaneous acceleration as a function of time, position, and velocity. In the dynamic method a nominal trajectory (satellite position as a function of time) is generated by analytically or numerically integrating the acceleration model. The orbit solution is compared with the one predicted by the observations. Selected parameters of the force models acting on the satellite may be adjusted along with an initial satellite position and velocity in the batch least-squares estimation[7] technique in order to minimize the difference between the actual observations and the predicted ranges (O-C residuals). Accuracy of the dynamic orbit determination approach is highly dependent on the satellite force models. Thus the accuracy of orbit determination may be reduced if the satellite forces are mis-modelled. Figure 10 illustrates a schematic representation of the dynamic orbit determination technique.

[7] Least squares estimation is a mathematical algorithm that uses definitive deterministic force models to minimize the RMS of measured O-C residuals. It consist of a sequence of linear LS corrections. A weighting factor is applied to each residual, and it is the square of the weighted residuals, which is minimized.

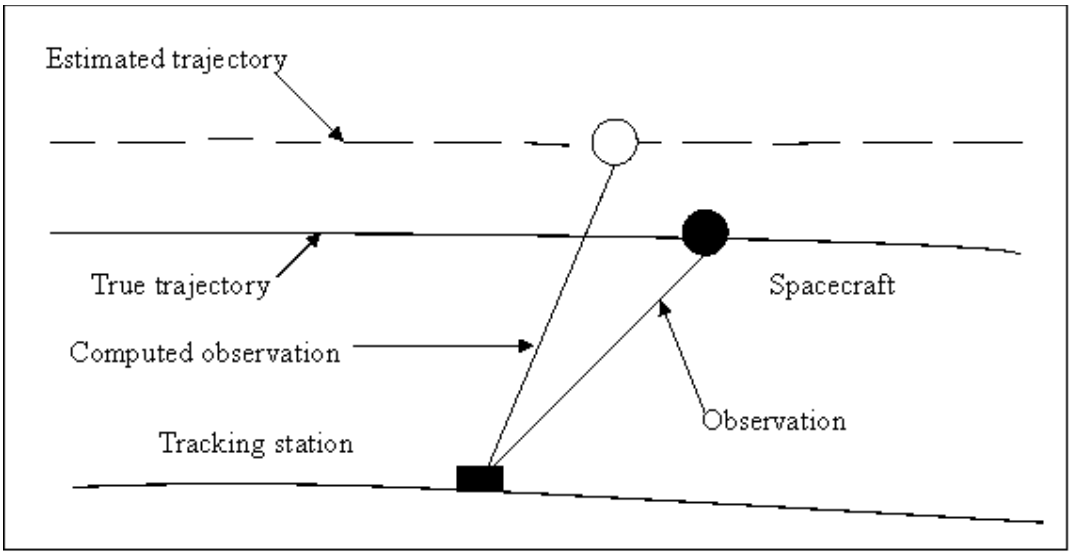

Figure 10. The orbit estimation problem (adopted from Yunck, 1997)

The basic equation describing the motion of an orbiting satellite is given by Equation (58),

$$\ddot{\vec{r}} = -\frac{GM}{r^3}\vec{r} + k_s, \tag{58}$$

where $\ddot{\vec{r}}$ is the acceleration vector of the satellite, $\vec{r}$ is the geocentric position vector of the satellite and k_s represents the sum of all the perturbing accelerations acting on the satellite, where

$$k_s = \ddot{r}_E + \ddot{r}_s + \ddot{r}_m + \ddot{r}_e + \ddot{r}_o + \ddot{r}_D + \ddot{r}_{SP} + \ddot{r}_A . \tag{59}$$

In Equation (59), $\ddot{r}_E$ is the perturbing forces due to the non-spherically and inhomogeneous mass distribution within the Earth system, $\ddot{r}_s$ and $\ddot{r}_m$ are the perturbing forces due to the Sun and the Moon respectively, $\ddot{r}_e$ and $\ddot{r}_o$ correspond to the perturbing forces as a result of the Earth and ocean tides respectively, $\ddot{r}_D$ is the atmospheric drag, $\ddot{r}_{SP}$ and $\ddot{r}_A$ correspond to Earth and solar radiation pressure respectively. A solution to Equation (58) can be obtained by using either analytical or numerical integration. However, for the purpose of precise orbit determination a numerical integration method is mostly preferred. Here, initial conditions (the position and velocity vector, $\left(r, \dot{\vec{r}}\right)$) at a time t_0 may be set as in Equation (60),

$$r(t_0) = r_0,$$
$$\vec{r}(t_0) = \vec{r}_0. \tag{60}$$

Double integration of Equation (58) using initial values of the orbit results yields a solution of the predicted orbit trajectory depicted in Equation (61),

$$r(t) = \iint \vec{r}(t)\,dt + \vec{r}_0 t + r_0\,. \tag{61}$$

The accuracy of the predicted orbit often depends on the epoch state ($r_0, \vec{r}_0$) and the acceleration model $\vec{r}(t)$ together with its physical parameters (Yunck, 1997). This can be achieved by using the least-squares method. Suppose that Z represents a vector of tracking data $(Z,...Z_n)^T$ made over an interval time (often known as the tracking arc). The task is to correct the initial values such that the nominal orbit given by Equation (61) shows a best fit to the pre-processed tracking data (e.g. the actual observations given by Z_i) with respect to the theoretical observations, $\bar{Z}_i$ derived from the solution trajectory. In other words, the aim is to obtain a trajectory $r(t)$ that minimizes a cost function expressed as in Equation (62),

$$J = \sum_{i=1}^{n} \left(Z_i - \bar{Z}_i\left[r(t)\right]\right)^2. \tag{62}$$

Theoretical observations $\bar{Z}_i$ can be obtained through linearization of Equation (62). This allows the differences $\delta Z_1 = Z_i - \bar{Z}_i$ to be formed. The differences in residuals are the observations to be used in a linear adjustment of the nominal trajectory. Let δZ represent the observable vector then the observation equation can be written as in Equation (63),

$$\delta Z = A\vec{x} + n\,. \tag{63}$$

In Equation (63), $\vec{x}$ is the vector of parameters to be estimated which include the six orbital elements $(a, e, i, \Omega, \omega, E)$ as well as adjustments to various dynamic and geometric model parameters, n is the random errors of the observable vector and A is a matrix of partial derivatives of the observations with respect to the elements of $\vec{x}$. Equation (63) is also known as the regression equation and its solution at the estimated epoch can be obtained by an iterative procedure. For further details on the regression equation, refer to Yunck (1997).

2.5.4.2. Kinematic orbit determination

The kinematic orbit determination is purely a geometric technique that depends only on GNSS (e.g. GPS) measurements and cannot be used by SLR. It does not take into account dynamic properties (e.g., gravity field, air drag, etc) of an orbiting satellite. Here the errors emanating from the satellite force models do not affect the accuracy of the kinematic orbit determination. Thus the accuracy is dependent on the availability and accuracy of GNSS data. In kinematic orbit determination the GNSS data are used to estimate the differences of the geometric coordinates, dx, dy and dz between the instantaneous a priori and the actual coordinates of the satellite (Colombo and Luthcke, 2004). The process is achieved by forming observation equations linearized about the a priori positions of the satellite. These equations are then solved to establish dx, dy and dz through a least-squares adjustment fit to the data and finally using the results to correct for the a priori positions. The kinematic orbit determination is mostly used during satellite manoeuvres when it is difficult to precisely describe the satellite dynamic forces using mathematical models (Colombo and Luthcke, 2004).

2.5.4.3. Reduced-dynamic orbit determination

In dynamic and kinematic methods the accuracy of a solution may be reduced due to mismodelling errors and GNSS measurement noise respectively. The reduced-dynamic technique (Yunck *et al*., 1994) may be defined as a method that exhibits half dynamic and half kinematic components and down-weights the errors caused by each method. In reduced-dynamic orbit determination the kinematic components of the dynamic force models are introduced in the form of the process noise model containing two parameters, the correlation time constant T which defines the correlation in the dynamic model error over one update interval and the dynamic model steady state variance V. The weighting of the kinematic and dynamic data is performed via the Kalman filter process noise at each step. When T is set to zero, and V is made large, the orbit determination method becomes kinematic, because deterministic components are not considered in the Kalman filter, and if T is large and V is zero the orbit determination method becomes dynamic, since the stochastic components are not estimated. Thus the reduced-dynamic orbit determination method is achieved by adjusting T and V to balance dynamic, geometric and measurement errors.

2.6. Global geopotential models

A number of spherical harmonic models have been developed over the years by different analysis centres. The development of such models could be attributed to the availability of terrestrial data as well as to the SLR tracking data of multiple satellites. Global Gravity field Models can be classified into three groups, namely, satellite-only, combined and tailored gravity field models (Amos and Featherstone, 2003). In the following a description of the various classes of geopotential gravity field models is provided.

2.6.1. Satellite-only GGMs

The satellite-only GGMs are primarily derived from the analysis of the orbits of tracked artificial Earth satellites. Numerous factors have been attributed to the degradation of the accuracy of the satellite-only models. These include:

a) Power-decay of the gravitational field with altitude,
b) The lack of continuous tracking data from the existing stations,
c) Precession of the Earth-based range measurements to the satellites (as a result of atmospheric refraction),
d) Difficulties in modelling non-gravitational and third body perturbations and,
e) Incomplete sampling of the global gravity field due to the limited number of satellite orbital inclinations available.

Due to these limitations gravity field models with high degree coefficients are often contaminated by noise.

2.6.2. Combined GGMs

The satellite-only models are often combined with terrestrial gravity data, and marine gravity anomalies computed by using satellite radar altimeter and airborne gravity data to yield high-degree (typically 360) combined GGMs. The combined GGMs are subject to the same deficiencies as in satellite-only GGMs. In addition, the combined gravity models are limited in precision due to the poor spatial coverage and the quality of the additional data used as well as other errors emanating from terrestrial gravity anomalies (Heck, 1990). A typical example is the long-wavelength errors in terrestrial gravity anomalies caused by distortions in and offsets among different vertical geodetic datums reported in e.g., Heck (1990).

2.6.3. Tailored GGMs

In tailored gravity field models the spherical harmonic coefficients of the satellite-only models or the combined models are often adjusted and extended to higher degrees by using higher resolution gravity data that may have not necessarily been used previously (Wenzel 1998). This is normally achieved using integral formulas to derive corrections to the existing geopotential coefficients, as opposed to the combination at the normal equation level that is used to construct combined GGMs. Tailored GGMs are only applied over the area in which the tailoring was applied, because spurious effects can occur in areas where no data are available (Kearsley and Forsberg, 1990).

2.6.4. Some remarks on the classification of gravity field models

A number of GGMs have been derived by different groups around the world. These models include the Ohio State University (OSU) series, GeoForschungs Zentrum (GFZ) Potsdam series, Goddard Earth Models (GEM) series, Joint Gravity Models (JGM) series, Texas Earth Gravity (TEG) models, GRIM (GRGS and German Geodetic Research Institute Munich) models and European Improved Gravity model of the Earth by New techniques (EIGEN) models. All the published models have been made available to the scientific community and are freely available to the public for example at the International Centre for Global Earth Models on http://icgem.gfz-potsdam.de/ICGEM. A review of gravity field models derived between 1970 and 1997 can be found in Rapp (1998). Here only developments undergone in the gravity field modelling for the last two decades (e.g., 1990 – 2010) are discussed. Characteristics of these models are summarized in Table 2.

Table 2. Summary of some of the GGMs released between 1990 and 2008. Data: S=satellite tracking data, G = gravity data, A = altimetry data. Geophysical applications of these models include gravity field, satellite orbit determination, station coordinates, reduction of altimeter data, Earth rotation and computation of geoid undulations.

Model	Year	Deg.	Data	Reference
GRIM4C1	1990	50	S, G, A	Schwintzer *et al*. (1991)
OSU91A	1991	360	GEMT2, G, A	Rapp *et al*. (1991)
JGM3	1994	70	S, G, A	Tapley *et al*. (1996)
GRIM4-S4	1995	70	S	Schwintzer *et al*. (1997)
GRIM4-C4	1995	72	S, G, A	Schwintzer *et al*. (1997)
GFZ96	1996	359	PGM055, G, A	Gruber *et al*. (1997)
EGM96	1996	360	EGM96S, G, A	Lemoine *et al*. (1998)
GRIM5C1	1999	120	S, G, A	Gruber *et al*. (2000)
EIGEN-1	2002	119	S (CHAMP)	Reigber *et al*. (2002)
EIGEN-2	2003	140	S (CHAMP)	Reigber *et al*. (2003)
GGM02S	2004	160	S (GRACE)	Tapley *et al*. (2005)
GGM02C	2004	200	S (GRACE), G, A	Tapley *et al*. (2005)
EIGEN-GL04S1	2006	150	S (GRACE, LAGEOS)	Foerste *et al*. (2006)
EIGEN-GL04C	2006	360	S (CHAMP, GRACE), G, A	Foerste *et al*. (2006)
EIGEN-5S	2008	150	S (GRACE, LAGEOS)	Foerste *et al*. (2008)
EIGEN-5C	2008	360	S (CHAMP, GRACE), G, A	Foerste *et al*. (2008)
EGM2008	2008	2190	S (GRACE), G, A	Pavlis *et al*. (2008)

The first considered model is a combined gravity field model, GRIM4C1 reported by Schwintzer *et al*. (1991). This model was computed as a joint collaboration between DGFI and GRGS. The GRIM4C1 model was derived up to degree and order 50 in terms of spherical harmonics. It incorporated GRIM4S1 satellite-solution, mean gravity anomalies and Seasat altimeter derived mean geoid undulations. The OSU91A geopotential model was reported by Rapp *et al*. (1991). This model was an upgraded version of OSU89a and OUS89b. It was computed complete to degree and order 360 in terms of spherical harmonics in a blended form. In the computation of the OSU91A, coefficients to degree 50 were based on a combined solution from GEM-T2 model, surface gravity data and GEOSAT altimeter data. The remaining coefficients (51-360) were derived from a combined solution computed from terrestrial data, altimeter derived anomalies and the topographic anomalies.

The Joint Gravity Model 3 (JGM3) model released in 1994 was reported by Tapley *et al*. (1996). This model was developed by NASA/GSFC and the University of Texas at Austin as part of the Topex Poseidon (T/P) project. This combined model was derived by adding the

geopotential coefficients from the pre-launch model, JGM1 and their associated error covariance with GPS, SLR, DORIS tracking of T/P, laser ranging tracking of LAGEOS 2 and Stella and DORIS tracking of SPOT 2. The model was derived complete to degree and order 70. The GRIM4-S4 and GRIM4-C4 reported by Schwintzer *et al.* (1997) were developed as a joint collaboration between GFZ Potsdam and GRGS Toulouse/Grasse for requirements of geodetic and altimeter satellite missions. The GRIM4-S4 model was derived solely from satellite tracking data complete to degree and order 70. On the other hand, the GRIM4-C4 model was derived based on a least squares adjustment involving a combined solution from the GRIM4-S4 model and surface gravity data from gravimetric and altimeter measurements. This model was computed complete to degree and order 72, corresponding to a spatial resolution of 555 km at the surface of the Earth (Schwintzer *et al.*, 1997). The GRIM4-S4 and GRIM4-C4 models were thought to be efficient for satellite orbit computations especially with orbit altitudes exceeding about 800 km (Schwintzer *et al.*, 1997). The GFZ96 geopotential model, which was an upgrade of the GFZ93 and GFZ95 models, was reported to provide high resolution of GFZ derived models (Gruber *et al.*, 1997). This combined model was computed from the then improved terrestrial data derived from a 3-year ERS-1 mean sea surface and PMG055 solution. The solution was also combined with altimeter derived gravity anomalies and normal equations and potential coefficients of the GRIM4-S4 model as the *a priori* model. The GFZ96 model was derived to degree and order 359.

Lemoine *et al.* (1998) described the combined spherical harmonic model, EGM96, which is complete to degree and order 360 and corresponds to a global resolution of about 55 km. The EGM96 model was developed based on a joint collaboration between NASA Goddard Space Flight Centre (GSFC), the National Imagery and Mapping Agency (NIMA) and the Ohio State University (OSU). This is a blend model were three computational procedures were used. The spherical harmonic coefficients from 2-70 were derived based on a least squares adjustment involving satellite tracking data, terrestrial data and altimeter data of the ocean surface from the T/P, ERS-1, and GEOSAT missions and fill-in gravity anomalies in areas lacking data (Amos and Featherstone, 2003). From degree 71-359 the coefficients were computed from a combined solution based on normal equations derived from the satellite tracking data which were used as a priori values. The remaining coefficients at degree 360 were taken from a quadrature combined solution derived from the a priori satellite model and ERS-1/GEOSAT altimeter-derived

anomalies. The EGM96 geopotential model was believed to provide a more accurate reference surface for the topography as well as improve orbit determination for low orbiting satellites (Lemoine *et al*., 1998). The GRIM5C1 gravity field model reported by Gruber *et al*. (2000) was derived in a German-French joint collaboration between GFZ Potsdam and GRGS Toulouse. The model was computed up to degree and order 120. It incorporated terrestrial and airborne mean gravity anomalies, altimetric gravity anomalies from NIMA and mean gravity anomalies derived from the GRIM5S1 model.

Most of the geopotential models released from 2000 onwards are derived solely from CHAMP, GRACE and GOCE missions plus other satellites, terrestrial and altimeter data. Geopotential models generated from the inclusion of the three satellite missions data are believed to be more accurate when compared with the prior models (e.g., they allow, with an unprecedented accuracy and resolution, the recovery of the mean sea surface topography from the difference between an altimetry-based mean sea surface height model and the gravity model's derived geoid) (Dobslaw *et al*. 2004). The first CHAMP geopotential model, EIGEN-1 reported by Reigber *et al*. (2002) was derived in a German-French joint collaboration complete to degree and order 119. This model was derived by use of GPS tracking and three months on-board accelerometer data from CHAMP. The EIGEN-1 geopotential model was reported to resolve the geoid and gravity with an accuracy of about 20 cm and 1 mGal respectively at a half-wavelength resolution of 550 km (Reigber *et al*., 2002). The EIGEN-2 model reported by Reigber *et al*. (2003) was also derived in a collaboration between Germany and France. This satellite-only model was derived complete to degree and order 140. The model incorporated gravity orbit perturbations, exploiting GPS CHAMP satellite-to-satellite tracking and six months on-board accelerometer data. The accuracy in terms of geoid and gravity for the EIGEN-2 model was reported to be about 10 cm and 0.5 mGal respectively.

Similar to the CHAMP mission, the GRACE mission data set has enabled a homogeneous determination of the geopotential gravity field modelling. The first is the satellite-only model, GGM01S reported by Tapley *et al*. (2004b). The model derived to complete degree and order 120 incorporated GRACE tracking data spanning April to November 2002 adding to a total of 111 selected days and using least squares adjustment. The authors reported an error estimate accuracy of about 2 cm over the land and ocean regions. An improved geopotential model to GGM01 called GGM02 was released in 2005. This model exists both in the GRACE

based satellite-only, GGM02S and the combined model, GGM02C (Tapley *et al*. 2005). The combined geopotential model incorporated the GRACE-only model GGM02S with EGM96 plus 14 months of GRACE data spanning April 2002 to December 2003. It was computed to maximum degree and order of 200 in terms of spherical harmonics. Improvements by a factor of two were reported with error estimates of less than 1 cm geoid height to spherical harmonic at degree 70.

The satellite-only model, EIGEN-GL04S1 described by Foerste *et al*. (2006) has a maximum degree and order of 150. It incorporated GRACE-only (EIGEN-GRACE04S) and GRACE/LAGEOS (EIGEN-GL04S) solutions. EIGEN-GL04S1 was later combined with surface gravity data from altimetry over the oceans and gravimetry over the continents to derive a high resolution gravity model EIGEN-GL04C released in 2006 (Foerste *et al*., 2006). This combined gravity field model is an outcome of the joint gravity field processing between GRGS Toulouse and GFZ Potsdam. The satellite-part of EIGEN-GL04C is based on GRACE and LAGEOS data and the maximum degree and order of this model is 360 in terms of spherical harmonics. The EIGEN-5C model reported by Foerste *et al*. (2008) was also a joint collaboration between GFZ Potsdam and GRGS Toulouse. It is an upgrade of EIGEN-GL04C and has a maximum degree and order of 360. The model is again a combination of GRACE and LAGEOS tracking data combined with addition of gravimetry and altimeter surface data. Combination of the satellite and surface data have been done by combining normal equations obtained from observation equations for the spherical harmonic coefficients. The National Geospatial-Intelligence Agency (NGA) released the first ever global model capable of resolving the Earth's gravity field beyond spherical harmonic degree 2000, a model called EGM2008. A description of this model can be found in Pavlis *et al*. (2008). The EGM2008 gravity field model has a maximum degree and order of 2159. It incorporates improved gravity anomaly data, altimetry-derived gravity anomalies and GRACE based satellite solutions. It allows proper computation of quasigeoid heights, gravity anomalies and vertical deflections and has a spatial resolution of ~5 arc minutes or ~9 km in the latitudinal direction (Pavlis *et al*., 2008).

2.7. Concluding remarks

The continuous design and deployment of satellite missions dedicated to gravity field measurements and the availability of high-precision data have led to the availability of gravity

information with unprecedented spatial-temporal resolution and accuracy. In particular, the advent of satellite data has made it possible to determine the gravity field of the Earth via modelling. To this end, these data sets are the basis for robust gravity field modelling with more than 100 gravity field models released in the scientific community since the early 1960s. Different gravity field models could be characterized by various degrees of spatial-temporal resolution. Despite the many scientific milestones in gravity field modelling, a study evaluating many of the developed gravity field models in the context of POD by use of SLR data have remained inconclusive. In particular, there has not been new SLR analysis software with the capability of POD with sensitivity analysis of gravity field model options. The research work reported in this thesis demonstrates the capability of the SDAS package to investigate the contribution of the different gravity field models applied in POD.